

Microscopic Dynamics and Transport of Hydrogen in Proton Conducting  
Oxides

Erik J. Spahr

Williamsburg, Virginia

Master of Science, College of William and Mary, 2007

Bachelor of Science, Mary Washington College, 2004

A Dissertation presented to the Graduate Faculty  
of the College of William and Mary in Candidacy for the Degree of  
Doctor of Philosophy

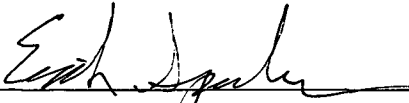
Department of Physics

The College of William and Mary  
January 2011

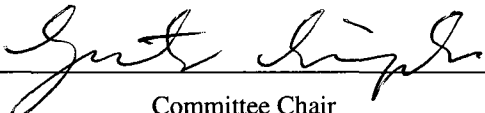
**APPROVAL PAGE**


This Dissertation is submitted in partial fulfillment of  
the requirements for the degree of


Doctor of Philosophy


  
\_\_\_\_\_  
Erik J. Spahr


Approved by the Committee, August 2010

  
\_\_\_\_\_  
Committee Chair  
Professor Gunter Lüpke, Applied Science  
The College of William and Mary

  
\_\_\_\_\_  
Professor William E. Cooke, Physics  
The College of William and Mary

  
\_\_\_\_\_  
Professor William J. Kossler, Physics  
The College of William and Mary

  
\_\_\_\_\_  
Professor Henry Krakauer, Physics  
The College of William and Mary

  
\_\_\_\_\_  
Professor Robert L. Vold, Applied Science  
The College of William and Mary

## ABSTRACT PAGE

The microscopic motion of hydrogen in solid oxides plays an important role in defect migration and reaction processes. Understanding the vibrational dynamics associated with both hydrogen-oxygen (O-H) bonds and the surrounding ionic environment allows one to better characterize these fundamental interactions. This thesis presents a comprehensive investigation into the vibrational decay dynamics of O-H and O-D stretch modes in crystalline oxides using time-resolved infrared pump-probe spectroscopy.

Measurements of the vibrational lifetimes of hydrogen related local modes in potassium tantalate ( $\text{KTaO}_3$ ) and titanium dioxide ( $\text{TiO}_2$ ) show that the localized O-H vibration is very closely tied to proton transport. In  $\text{KTaO}_3$  we find the lifetimes to be on the order of a few hundred picoseconds and determine that the vibrational decay is due to a lattice-assisted tunneling process. Furthermore, we identify the assisting phonon and extract the excited-state tunneling rate. In  $\text{TiO}_2$  we measure the lifetimes at only a few picoseconds. Here, the decay can be described by a classical hopping process. In both cases the absorption-stimulated transfer rate is found to be dramatically larger than spontaneous or thermally activated proton transfer.

These studies provide valuable information regarding the details and fundamentals of hydrogen-lattice interactions in solid oxides. Such insight is valuable for better understanding the role of hydrogen in materials important for a variety of applications ranging from optoelectronics to alternative energy technologies.

For my parents, John and Nancy Spahr and my wife, Aiyana.

## TABLE OF CONTENTS

	Page
<b>Acknowledgements</b> . . . . .	<b>viii</b>
<b>List of Tables</b> . . . . .	<b>ix</b>
<b>List of Figures</b> . . . . .	<b>x</b>
<b>CHAPTER</b>	
<b>1 Introduction</b> . . . . .	<b>2</b>
1.1 Hydrogen in Solid Oxides . . . . .	3
1.2 Hydrogen Transport and Vibrational Dynamics . . . . .	7
1.2.1 Transport Mechanisms . . . . .	7
1.2.2 Local Vibrational Dynamics . . . . .	9
1.2.3 Theoretical Work . . . . .	12
1.3 Outline . . . . .	13
<b>2 Theoretical Considerations</b> . . . . .	<b>14</b>
2.1 Potential Energy Surface and Anharmonicity . . . . .	14
2.1.1 Double Morse Potential . . . . .	16
2.2 Infrared Linewidth and Broadening Mechanisms . . . . .	17
2.3 Vibrational Decay Mechanisms . . . . .	18
2.3.1 Multiphonon Relaxation . . . . .	18
2.3.2 Proton Tunneling . . . . .	22

2.3.3	Proton Hopping . . . . .	26
<b>3</b>	<b>Experimental Details . . . . .</b>	<b>30</b>
3.1	Fourier Transform Infrared Absorption Spectroscopy . . . . .	31
3.2	Laser System and Vibrational Lifetime Measurements . . . . .	35
3.2.1	Laser System . . . . .	35
3.2.2	Measuring Vibrational Lifetimes . . . . .	36
3.3	Materials . . . . .	39
3.3.1	Sample Preparation . . . . .	41
<b>4</b>	<b>Proton Tunneling in <math>\text{KTaO}_3</math> . . . . .</b>	<b>43</b>
4.1	Proton Tunneling: a Vibrational Decay Channel . . . . .	44
4.2	Vibrational Lifetimes and Reverse Isotope Effect . . . . .	46
4.3	Lifetime Temperature Dependence . . . . .	49
4.4	Phonon-Assisted Proton Tunneling . . . . .	51
4.5	Summary and Conclusions . . . . .	54
<b>5</b>	<b>Photon-Stimulated Proton Hopping in <math>\text{TiO}_2</math> . . . . .</b>	<b>56</b>
5.1	Rutile $\text{TiO}_2$ : a Model System . . . . .	57
5.2	Vibrational Lifetime Measurements . . . . .	58
5.3	Phonon-Assisted Hopping . . . . .	62
5.3.1	Energy Barrier . . . . .	63
5.4	The Photo-Enhanced Hydrogen Transport Effect . . . . .	65
5.5	Summary and Conclusions . . . . .	66
<b>6</b>	<b>Summary and Outlook . . . . .</b>	<b>67</b>
6.1	Summary . . . . .	67
6.2	Outlook . . . . .	69

<b>APPENDIX A</b>	
<b>Laser System Details</b>	<b>75</b>
A.1 Picosecond high power laser pulses	75
A.2 Tunable infrared picosecond pulses	77
A.2.1 Energy Conservation, Phase Matching and Tuning	78
A.2.2 TOPAS	78
A.2.3 Difference Frequency Generation	79
<b>Bibliography</b>	<b>81</b>
<b>Vita</b>	<b>88</b>

## ACKNOWLEDGMENTS

It has been my pleasure to enjoy the company of many helpful and encouraging researchers in both the Physics and Applied Science departments at the College of William and Mary over the past several years. Above all, I wish to express my sincere appreciation and gratitude to my advisor, Prof. Gunter Lüpke who has given me continual support and expert advice throughout my graduate school experience. Without his guidance, this dissertation would not have been possible.

Additionally, this research project has involved several valuable collaborations. I would like to thank Prof. Michael Stavola and Lanlin Wen at Lehigh University for their high-resolution infrared absorption measurements as well as their general experimental insight and analysis regarding absorption spectra. I would also like to thank Dr. Lynn A. Boatner and his group at Oak Ridge National Lab for growing and annealing the single crystal samples examined in this dissertation. I also acknowledge Dr. Leonard C. Feldman and Dr. Norman H. Tolk for their input while preparing and editing our manuscripts for publication.

I would also like to thank my fellow group members for always lending a hand the lab and being available to bounce around ideas or concerns. Working with them has been a continual learning experience.

I would also like to express my sincere thanks to my committee members: Dr. William E. Cooke, Dr. William J. Kossler, and Dr. Henry Krakauer of Physics, and Dr. Robert L. Vold of the Applied Science Department. I appreciate them taking the time to attend several annual reviews, look over my dissertation and provide instructive comments and criticisms.

I would also like to thank Scott Owen and the Daily Grind for providing countless scones and cups of coffee. Having a nice place to refuel and relax is just as important as having a supporting work environment.

Lastly, but most importantly I thank my wife Aiyana and my parents John and Nancy for their belief, encouragement, and love.

## LIST OF TABLES

Table	Page
6.1 Known hydrogen complexes in various oxides including isotopic shifts, where available. Measurements are included from this thesis and are labeled as “current work” (CW). Those defects labeled with a V represent vacancy associates. For example, the $V_{OH}$ represents a OH group occupying the region adjacent to a Magnesium vacancy. . . . .	74

## LIST OF FIGURES

Figure	Page
1.1 Proton transport in an electrochemical cell electrolyte. This process can be used to produce electricity from hydrogen (fuel cell) or for hydrogen extraction from hydrocarbons such as methane. . . . .	4
1.2 Examples of hydrogen incorporation into a generic oxide lattice. . . . .	5
1.3 Proton (red) migration mechanism in an oxide ion (blue) lattice. . . . .	8
1.4 Double-Morse potential well for proton in an oxide host. At equilibrium the proton is localized about at a minima near an oxygen atom. The horizontal blue lines represent the vibrational energy levels of the O-H stretch mode. The dashed curve indicates the change in potential energy due to lattice vibrations. . . . .	9
1.5 Schematic illustrations of O-H LVMS. The solid circle represents the hydrogen ion and arrows indicate the direction of oscillation. . . . .	10
2.1 General representation of the Double Morse Potential. . . . .	16
2.2 Calculated lifetime temperature dependence for a decay into $N$ phonons using Eq. (2.12). . . . .	21
3.1 A Michelson-Morley interferometer for FTIR spectroscopy. . . . .	32
3.2 Hydrogen and deuterium related stretch modes in rutile $\text{TiO}_2$ identified by FTIR absorbance spectroscopy at 10K. . . . .	34
3.3 Top-down schematic of the picosecond laser system used in this work. . .	36

3.4	Schematic of experimental pump-probe setup used in this work. . . . .	37
3.5	Two photon signal from a Ge reference sample used to find the temporal overlap of the pump and probe beams. . . . .	38
3.6	Probe spectrum passing through $\text{KTaO}_3$ at 80k. Dip at 3883.8 nm ( $2575 \text{ cm}^{-1}$ ) corresponds to the O-D stretch mode. . . . .	39
4.1	The ionic configuration around the proton in a perovskite lattice. (a) The proton moves throughout the oxygen octahedral network. (b) the potential energy diagram of the hydrogen atom, tunneling from one well to another. The vibrational ground and first excited state are shown in the left-hand well of the DMP. The inset indicates the vibrational modes associated with phonon-assisted tunneling. . . . .	44
4.2	The O-H and O-D stretch modes in $\text{KTaO}_3$ identified by FTIR. Fits to a Lorentzian lineshape give linewidths shown in the inset. . . . .	45
4.3	Transient bleaching signal, $S_b$ of the O-H and O-D stretch modes in $\text{KTaO}_3$	46
4.4	FTIR spectra taken after consecutive anneals at elevated temperatures (degrees Celsius) identifying the O-H wag mode. . . . .	48
4.5	Temperature dependence of the O-H and O-D stretch mode lifetimes . . .	50
4.6	Experimental proton tunneling rate, $k_{PT}$ , extracted from the vibrational lifetimes of the O-H and O-D stretch modes. The solid line is a fit to Trakhtenberg's model. . . . .	52
4.7	Estimated ground state (GSPT) and excited state (ESPT) tunneling rates in $\text{KTaO}_3$ according to Trakhtenberg's model. . . . .	54

5.1	Ionic configuration for the proton in the $\text{TiO}_2$ lattice. (a) The rutile structure is shown here to emphasize the characteristic open $c$ channel. Small arrows represent the vibration of the stretch and wag modes, while the dashed arrow indicates the reaction pathway for proton migration. (b) A schematic representation of the potential surface for the proton in the $c$ channel. The horizontal lines depict vibrational levels for the O-H stretch mode. . . . .	58
5.2	Vibrational lifetimes of the O-D and O-D stretch modes. (a) The O-D transient bleaching signal is fit to a single exponential decay giving a lifetime of 5.41 ps and is in excellent agreement with the IR linewidth in Fig. 5.3. (b) The black circles indicate the O-H stretch mode measurement of approximately 1.5 ps. The gray squares indicate an off-resonant measurement representative of the laser pulse width. Note that the $T_1$ values measured here are much shorter than in $\text{KTaO}_3$ . . . . .	59
5.3	Infrared absorption spectra of the O-D (a) and O-H (b) stretch modes in rutile $\text{TiO}_2$ . The spectra are fitted with a Lorentzian line shape to yield FWHM values shown in the inset. These linewidths are in excellent agreement with the measured lifetimes using the relation in equation (5.1). . . . .	60
5.4	Temperature dependence of the O-D lifetime (blue circles) along with the O-H lifetime (black diamonds) extracted from the vibrational linewidth. Both data sets are fitted to a model for a lattice-assisted proton transfer process. . . . .	61
5.5	Infrared linewidths (FWHM) for O-H, O-D, and O-T stretch modes in $\text{TiO}_2$ measured at 10 K plotted against photon energy. The points shown are for the transitions $\nu(\text{OT})_{01}$ , $\nu(\text{OD})_{01}$ , $\nu(\text{OH})_{01}$ , $\nu(\text{OH})_{\text{comb}}$ , and $\nu(\text{OH})_{02}$ with increasing energy, where subscripts indicate the vibrational quantum number. Absorption lines for the O-H combination and overtone modes are shown in the inset. . . . .	64
6.1	Absorption spectra of the O-H stretching region of a polycrystalline electrolyte material. . . . .	70
6.2	Vibrational lifetime of the O-H stretch mode in $\text{ZnO}$ at 10 K. . . . .	71

6.3	Preliminary temperature dependence of the $3326\text{ cm}^{-1}$ line in ZnO. Solid line is a fit to a two phonon decay process according to equation (2.13) . . .	72
6.4	Lifetime of the $V_{OH}$ stretch mode in MgO measured at 10 K. . . . .	73
6.5	Temperature dependence of the $V_{OH}$ center in MgO. . . . .	73
A.1	Autocorrelation measurement of the TITAN pulse time. . . . .	76
A.2	TOPAS optical layout. . . . .	80

MICROSCOPIC DYNAMICS AND TRANSPORT OF HYDROGEN IN PROTON  
CONDUCTING OXIDES

# CHAPTER 1

## Introduction

The solid oxides are an important class of materials that have attracted considerable interest for a wide range of technological applications including microelectronics, photovoltaics, and optoelectronics. Understanding the microscopic dynamics of hydrogen-related defects in oxides is not only crucial for the further understanding of basic material properties, but also relevant for the continual development of these important technologies. For example, the science behind fuel cells, photo-catalysis, hydrogen storage and sensing stems from a basic knowledge of how protons move through these materials. On what timescale does a hydrogen defect dissociate from a stable position? What role do the surrounding atoms play in migration? How can we improve proton diffusion and conduction? The current investigation of hydrogen dynamics explores these important questions and suggests a new approach for improved hydrogen transport in solid oxides.

## 1.1 Hydrogen in Solid Oxides

The role of hydrogen defects in oxides must not be overlooked. Hydrogen is present in almost all material growth and preparation techniques – even in high vacuum environments. Sometimes hydrogen is introduced intentionally to achieve certain characteristics or passivate unwanted electrical states. In semiconducting oxides, hydrogen often acts as an amphoteric impurity with the undesired effect of counteracting the prevailing conductivity. However, in some cases such as in ZnO and SnO<sub>2</sub> hydrogen has been shown to act as a shallow donor [1] and contribute to the n-type conductivity. Such transparent conducting oxides (TCOs) are commonly deposited as thin films on glass for flat panel displays, photovoltaic arrays, and other optoelectronic applications. Others TCOs such as TiO<sub>2</sub> are suitable as photo-anodes for electrolytic production of hydrogen directly from sunlight [2]. Clearly, a fundamental understanding of hydrogen defect incorporation is crucial.

Recently, the wide band-gap semiconductor ZnO ( $E_g = 3.3$  eV) has also attracted considerable interest as a blue/UV light emitter. The high excitonic binding energy makes it a promising alternative to the commonly used GaN [3]. The main dilemma however, is that it is difficult to achieve p-type ZnO, and the sources of inherent n-type conductivity – including hydrogen – are of great interest. Hydrogen is also a common impurity in other wide band-gap oxides such as MgO and HfO<sub>2</sub>, which have a high dielectric constant, and are thus potential candidates to replace SiO<sub>2</sub> as a high- $\kappa$  gate dielectric in computer processors. In these materials, hydrogen is often introduced during post-deposition anneals and may be a source of positive charge traps which can decrease electron mobility in devices [4].

Perovskite-type oxides, which exhibit a wide range of interesting properties, usually

contain a high concentration of “as-grown” hydrogen defects. Applications of perovskite oxides range from high temperature superconductors such as YBCO ( $\text{YBa}_2\text{Cu}_3\text{O}_7$ ) to strongly correlated electron systems for spintronic devices [5]. Perovskites such as  $\text{BaTiO}_3$  and  $\text{Pb}(\text{Zr}, \text{Ti})\text{O}_3$  exhibit piezoelectric and ferroelectric properties which make them suitable for tunable capacitors and ferroelectric nonvolatile memory, and it is thought that hydrogen defects can cause unwanted leakage currents and loss of switchable polarization [4]. Other perovskite structured oxides are proton conducting and have catalytic properties which makes them useful for hydrogen electrochemical cell electrodes and electrolytes or for hydrogen production.

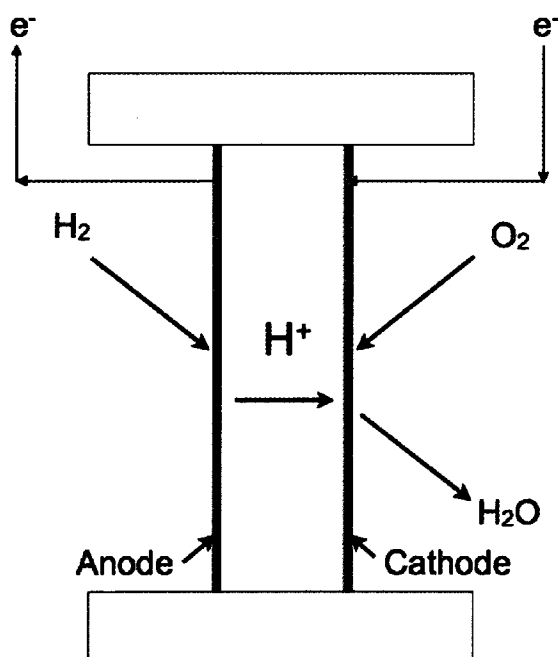


FIG. 1.1: Proton transport in an electrochemical cell electrolyte. This process can be used to produce electricity from hydrogen (fuel cell) or for hydrogen extraction from hydrocarbons such as methane.

One of the most clear cases to motivate the importance of hydrogen is that of the pro-

ton conducting oxides. In these materials, the positive hydrogen ion is the charge carrier for ionic conduction and moves throughout the atomic lattice of the host crystal. Consider the case of the hydrogen fuel cell, shown schematically in Fig. 1.1. Here, a catalytic reaction at the anode separates the electrons from their host proton. The electrons cannot pass through a proton conducting membrane (called an electrolyte) and are forced to drive an external electrical load. The protons then migrate through the electrolyte and recombine with their electrons at the cathode. The performance of this type of device depends largely on the proton transport efficiency in the electrolyte. Therefore, understanding the microscopic behavior of the proton-oxide interaction is crucial for the continual improvement of such devices.

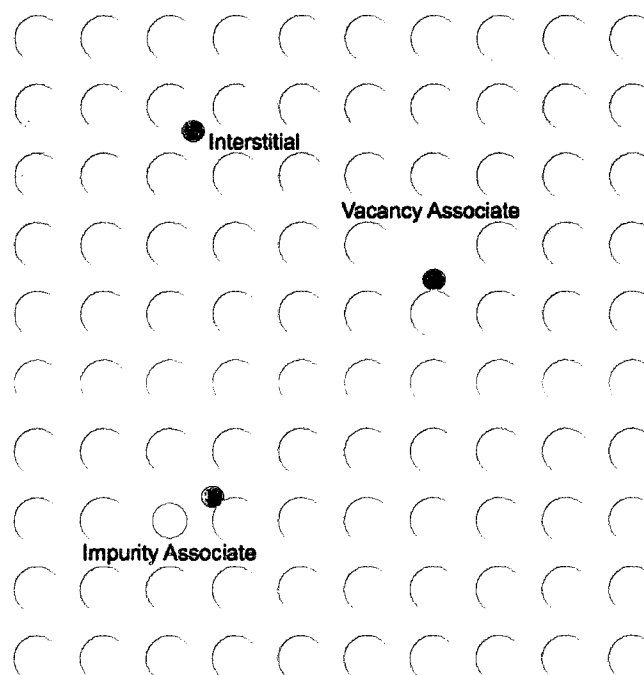


FIG. 1.2: Examples of hydrogen incorporation into a generic oxide lattice.

In oxides, hydrogen typically forms a covalent bond with one of the host oxygen

atoms forming a hydroxyl, or O-H, group. The orientation of this bond depends largely on the particular crystal structure and symmetry which varies highly from one oxide to the next. In most materials the O-H bond length is usually about one Angstrom ( $\text{\AA}$ ). In some cases, the O-H group can be associated with an atomic vacancy or a substitutional impurity ion – both of which can alter the vibrational characteristics of the oxygen-hydrogen system. An illustration of various hydrogen configurations in an oxide lattice is shown in Fig. 1.2.

In the present investigation, we focus on two crystalline materials: the perovskite oxide potassium tantalate ( $\text{KTaO}_3$ ) and rutile titanium dioxide ( $\text{TiO}_2$ ). The former is an ideal representative for the perovskites.  $\text{KTaO}_3$  is an established proton conductor and exhibits a simple cubic structure without any structural phase transitions at temperatures as low as a few Kelvin. Hydrogen diffusion in  $\text{KTaO}_3$  is therefore, isotropic. Rutile  $\text{TiO}_2$  was chosen to represent the transparent conducting (and similar) oxides. Hydrogen interaction with the rutile  $\text{TiO}_2$  surface and subsurface has been the subject of several recent studies investigating the photo-catalytic properties of  $\text{TiO}_2$  [6] [7]. In  $\text{TiO}_2$  hydrogen defects are very mobile, and unlike  $\text{KTaO}_3$ , diffusion in the rutile structure is anisotropic with preferred motion along the  $c$  direction. The structural difference between these two oxides results in a contrast between two hydrogen transport mechanisms and sets the stage for an interesting study in hydrogen defect dynamics.

## 1.2 Hydrogen Transport and Vibrational Dynamics

### 1.2.1 Transport Mechanisms

Hydrogen transport in oxides is unique in that the conducting ions are not native members of the oxide lattice. Rather, they are often referred to as hydrogen or O-H defects. Additionally, proton conduction in oxides is quite different from electronic conduction in metals. Proton conduction is not band like, but rather consists of hops between oxygen ions to which it temporarily bonds. Long range motion of the proton can be achieved by reorientations of the O-H bond direction in combination with transfers between two neighboring oxygen ions [8]. This sequential two step process is known as the Grotthuss mechanism [9]. This process is illustrated Fig. 1.3 for proton migration in an  $ABO_3$  perovskite oxide, where A and B represent generic ionic constituents.

Along the  $O - H \cdots O$  transfer direction, the local energy environment of the proton is often successfully modeled by a double-Morse potential well, illustrated in Fig. 1.4. If the energy of the proton is increased near the top of the double well barrier, it can pass from one minima to the other. This can be due to thermal or optical excitation. Vibrations of the surrounding oxygen ions can alter the potential shape so that vibration-assisted motion must also be considered. In addition to this classical hopping, the proton can also tunnel between neighboring oxygens. This quantum effect has been suggested both experimentally [10] and theoretically [11] and typically dominates at low temperatures.

Clearly, the O-H vibrational dynamics are very closely related to proton transport. For example, when the first vibrational level is populated (horizontal line in Fig. 1.4) the barrier height  $E_b$  is effectively lowered which will greatly increase the probability of thermal hopping or quantum tunneling. In some cases, the first vibrational excited state

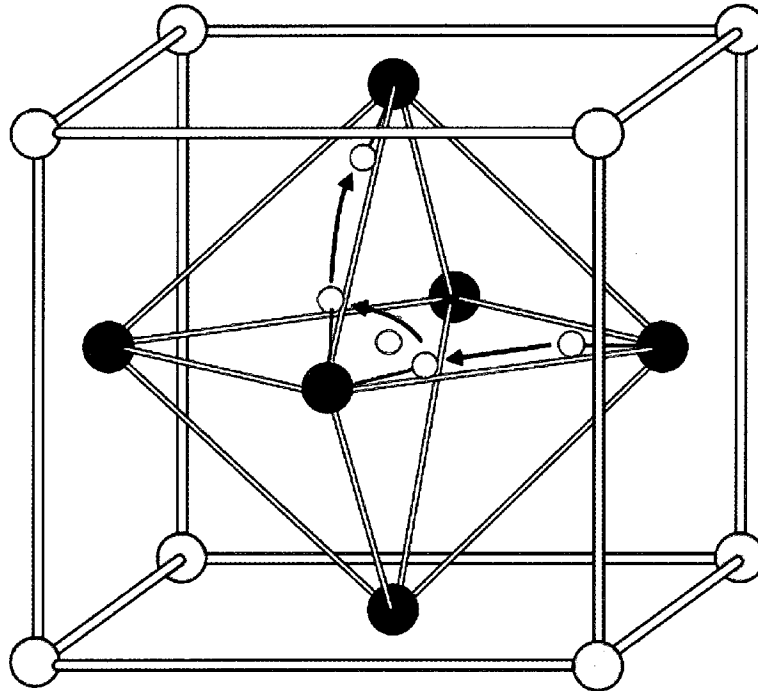


FIG. 1.3: Proton (red) migration mechanism in an oxide ion (blue) lattice.

may be close enough to the barrier height so that absorption may stimulate migration as has been suggested for hydrogen in ZnO [12].

Generally, hydrogen transport in oxides occurs at temperatures between 800-1000° C. This is the case for solid oxide fuel cells (SOFCs) – one of the more promising fuel cell designs due to their high efficiency and power output. Oxides used in SOFCs are often termed high temperature proton conductors (HTPCs). In such devices, thermal energy is needed to promote the proton over the potential well shown in Fig. 1.4. This requirement can cause significant problems such as thermal degradation and slow start-up times. It is therefore desirable to develop techniques that allow operation at lower operational temperatures, and a clear understanding of the microscopic proton dynamics and decay channels is a necessary step in this process [13].

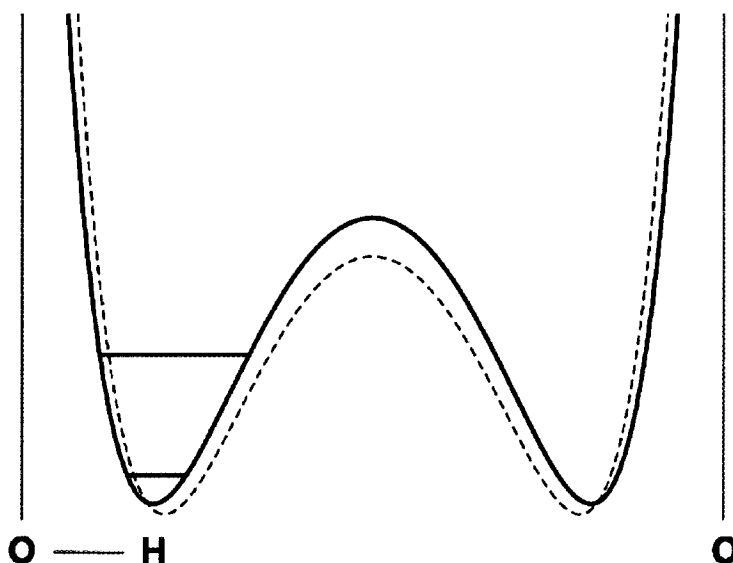


FIG. 1.4: Double-Morse potential well for proton in an oxide host. At equilibrium the proton is localized about at a minima near an oxygen atom. The horizontal blue lines represent the vibrational energy levels of the O-H stretch mode. The dashed curve indicates the change in potential energy due to lattice vibrations.

## 1.2.2 Local Vibrational Dynamics

In a bulk crystal, vibrations of the atomic lattice, or phonons, obey a certain dispersion relation characterized by a dependence of frequency ( $\omega$ ) on wavevector ( $\vec{k}$ ). This can be determined both experimentally from neutron scattering or theoretically from *ab initio* calculations. Usually, the vibrational frequency of these phonon modes range from a few wavenumber ( $\text{cm}^{-1}$ ) to about  $800 \text{ cm}^{-1}$ . Hydrogen defects in crystalline oxides are classified as local vibrational modes (LVMs) because their vibrational frequency is much higher than the bulk phonon modes and unlike lattice vibrations the LVMs cannot propagate throughout the entire lattice. In this work, typical O-H stretch modes are found to be around  $3,000\text{-}3500 \text{ cm}^{-1}$ .

Examples of common LVMs are the O-H stretch and wag (a.k.a. bend or libration)

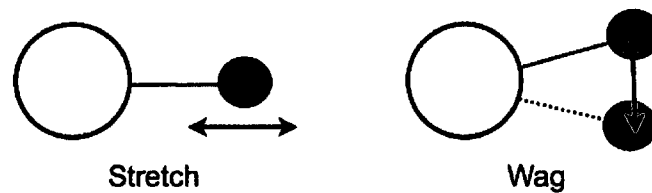


FIG. 1.5: Schematic illustrations of O-H LVMs. The solid circle represents the hydrogen ion and arrows indicate the direction of oscillation.

modes. These are illustrated in Fig. 1.5. After excitation, the transfer of vibrational energy can occur between two different local modes (e.g. from the stretch to the wag) or between a local mode and the bulk phonons. A comprehensive experimental study was performed by Baozhou Sun in his Ph.D. thesis (Applied Science, College of William and Mary) which analyzed the lifetimes of hydrogen related LVMs in Si and Ge [14]. A complementary theoretical molecular dynamics investigation was done by Dr. Damien West at Texas Tech University [15]. It was found that the lifetimes exhibit a remarkable structural dependence and that the decay process of stretch and bend modes can be quite different. In these systems, hydrogen stretch modes decay more readily to other localized modes or pseudo-localized modes involving atomic vibrations surrounding the defect. The low frequency wag modes, on the other hand, can more easily excite a specific set of bulk phonons—a process known as multiphonon relaxation. For such processes, the vibrational lifetime of the H related wag mode is related to the number of accepting phonon modes (decay order) through a universal frequency gap law, which states that the decay time increases exponentially with increasing order [16]. In Si and Ge, the covalent nature of the host crystal is quite different than the ionic atomic environment found in the oxides; therefore, one would expect the decay mechanisms to differ. Thus, identification of the O-H decay channel in oxides is important for a complete understanding of local

mode relaxation, diffusion mechanisms, and defect dislocation reactions in solids.

As alluded to above, hydrogen local modes are characterized by their vibrational frequency. Within a crystal lattice, an O-H group constitutes an electric dipole, which can be represented as a linear harmonic molecule. When light of a resonant frequency is incident on the dipole the energy will be absorbed and the O-H group will begin to oscillate. This simple principle is the basis behind the spectroscopic techniques used to identify and characterize hydrogen in oxides and semiconductors.

In this work a time-domain “pump-probe” transient bleaching technique is used to reveal vibrational decay times. Detailed analysis of these excited state vibrational lifetimes allows us to directly explore the microscopic dynamics of the hydrogen ion and the surrounding crystal lattice. Temperature dependent studies are particularly useful in determining how the O-H local vibration couples with the lattice because they allow one to essentially “freeze” out and control the phonon interaction. Such time resolved measurements are realized with the use of tunable, ultrafast lasers with pulse times on the order of a picosecond – a timescale appropriate for hydrogen vibrational dynamics in solids. To our knowledge, this thesis presents the first vibrational lifetime measurements of O-H related defects in oxide systems.

In addition to time domain measurements, Fourier transform infrared (FTIR) absorbance spectrometry is used to obtain static frequency domain information. FTIR is a standard tool for characterization of hydrogen related LVMs in solids and is commonly used to identify the local configuration and concentration of hydrogen in oxides and semiconductors [17]. Measurements of absorption peak-widths, temperature dependencies, and isotope shifts help spectroscopists determine the potential energy structure for localized vibrations in bulk materials. For example, exchanging an atom with a different isotope does not affect the chemical nature of the defect, but only changes the mass and

hence the vibrational frequency, allowing one to probe a different region of the local potential energy well. In the case of hydrogen with unit atomic mass, a deuterium substitution yields the largest mass contrast of all elements. The expected frequency shift can be understood in terms of a simple classical spring model by taking equal spring constants. The ratio of vibrational frequencies can be written as

$$\frac{\omega_H}{\omega_D} = \frac{\sqrt{1/m_H}}{\sqrt{1/2m_H}} = \sqrt{2}. \quad (1.1)$$

Thus, isotope substitution can be used to confirm that a particular IR spectral feature is indeed hydrogen related.

### 1.2.3 Theoretical Work

Hydrogen vibrational lifetime calculations in oxides are lacking. For the the covalently structured semiconductors, West and Estreicher have preformed first principles simulations of hydrogen and deuterium related modes in silicon and were able to correctly calculate the lifetimes for temperatures greater than 50 K and identify accepting phonon modes [18] [15]. Vibrational decay of O-H modes in ionic oxide crystals may differ and, unfortunately, a similar calculation in such systems does not yet exist. Hydrogen diffusion pathways and energy barriers, however, have been examined from a first principles approach in wurtzite ZnO [12] and in the perovskite BaZrO<sub>3</sub> [11], but these studies do not consider the lattice dynamics nor the local O-H vibration. Therefore the spectroscopic techniques utilized in this thesis provide unique, fundamental insight into the relaxation dynamics of hydrogen in solid oxides and are a starting point for further theoretical investigations.

## 1.3 Outline

The organization of the rest of this dissertation is as follows: in Chapter 2, I will overview the key theoretical considerations for this work. This includes the mathematical descriptions of vibrational linewidths and broadening mechanisms and the energetics of hydrogen in an oxide lattice. I will also overview three important vibrational decay channels: multiphonon relaxation, proton tunneling, and proton hopping.

In Chapter 3, I will discuss the experimental methods and techniques used in this work including details of FTIR spectroscopy and the pump-probe lifetime measurement technique, which also includes a brief description of the laser system. I will also describe the materials under examination and their technological and scientific importance.

In Chapter Chapter 4, I will present the O-H and O-D vibrational lifetime data for the perovskite oxide  $\text{KTaO}_3$ . The lifetimes are found to be extremely long at 400 ps for the O-D stretch mode, which is the longest lifetime ever reported for a hydrogen related defect in a solid. I will discuss the important findings, which identify proton tunneling as a dominant decay channel for the O-H stretch mode and show that the vibrational dynamics play an important role in the tunneling process.

In chapter Chapter 5, I show that vibrational excitation is closely related to proton migration in rutile  $\text{TiO}_2$ . Here the vibrational lifetimes are found to be short (1 – 5 ps) compared to those in  $\text{KTaO}_3$ . They reveal a fast coupling to the wag mode which is responsible for assisting in the hopping process.

Finally, in Chapter 6, I will summarize the key results and discuss future work and applications.

# **CHAPTER 2**

## **Theoretical Considerations**

This chapter provides an overview of the theoretical framework relevant to this thesis. The first section covers the general aspects related to the potential energy of a light ion in a host lattice, which is very important for determining reaction pathways related to proton diffusion or conduction. The second section reviews the important characteristics of FTIR absorption lines with particular attention paid to those related to the lifetime measurements. Finally, the last and most important section presents the mathematical background of three dominant vibrational decay channels for H local modes in solids.

### **2.1 Potential Energy Surface and Anharmonicity**

Understanding the dynamics of O-H local modes requires a detailed understanding of the potential energy surface occupied by the proton in the host lattice. This is especially important for describing transfer reactions that involve barrier crossing or penetration. A simple one-dimensional model commonly used to describe diatomic molecules is the

Morse potential [19]. Unlike a simple harmonic oscillator potential, the Morse potential does not have equal energy spacing and is known as an anharmonic well because the potential strength falls off at higher excited levels. The Morse potential can be written as

$$U(r - r_o) = D_e(e^{-2\beta(r-r_o)} - 2e^{-\beta(r-r_o)}) \quad (2.1)$$

where  $r_o$  is the equilibrium position,  $D_e$  is the dissociation energy, and  $\beta$  is a parameter describing the well width. The Morse potential is advantageous to work with because it has an exact solution to the Schrodinger equation given by

$$G(n) = \omega_e(n + 1/2) - \omega_e\chi_e(n + 1/2)^2 \quad (2.2)$$

where  $\omega_e = \beta(\hbar D_e/\pi c\mu)^{1/2}$  and  $\omega_e\chi_e = \hbar\beta^2/4\pi c\mu$  and  $\mu$  is the reduced mass of the oscillator [20]. The vibrational transition from the ground state to higher levels is defined by

$$\nu_{n0} = \Delta G_{n0} = G_n - G_0 = n\omega_e(1 - \chi_e(n + 1)) \quad (2.3)$$

and allows determination of the anharmonicity parameter,  $\omega_e\chi_e$ , from experimental observation of the overtone:

$$\chi_e = \frac{\nu_{20} - 2\nu_{10}}{2(\nu_{20} - 3\nu_{10})} \quad (2.4)$$

$$\omega_e = 3\nu_{10} - \nu_{20}. \quad (2.5)$$

It is also possible to determine the anharmonicity of a potential well from isotopic substitution. Different isotopic energies will sample a different point in the potential well. In this case the eigen-energies can be written in terms of the ratio of reduced masses of

the O-H, O-D, or O-T oscillator, and the anharmonicity parameters can be expressed in a similar manner to the overtone method above.

### 2.1.1 Double Morse Potential

A natural extension of the Morse potential is to describe the linear system of the O-H dipole and its interaction with a next near neighbor oxygen ion. This is referred to as a double Morse potential (DMP) and in oxides represents the system O-H $\cdots$ O. This simple model consists of two equivalent sites for the hydrogen and is often used in describing transfer reactions in which the proton moves between hosts. The mathematical representation is simply the sum of two back to back single Morse potentials from equation (2.1), given by  $V_{DMP} = U(r - r_1) + U(r_2 - r)$  where  $r_1$  and  $r_2$  are the positions of the two minima. Figure 2.1 shows a general representation where the dashed lines represent the two back to back single wells and the thick black line is their sum. Note that the barrier height is less than the dissociation energy for a single diatomic potential well.

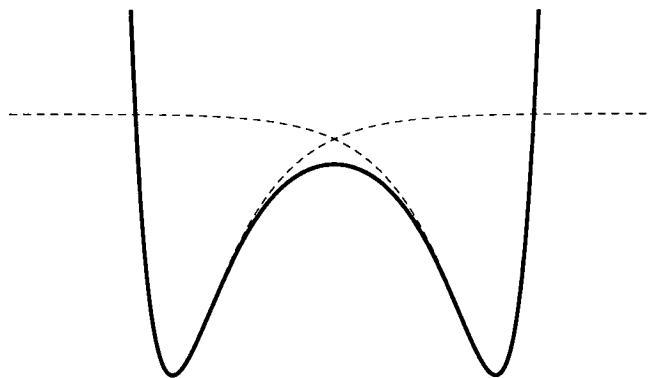


FIG. 2.1: General representation of the Double Morse Potential.

## 2.2 Infrared Linewidth and Broadening Mechanisms

Infrared absorption lines of LVMs in solids are characterized by their widths (FWHMs) and lineshapes. Two characteristic contributions to the homogeneous linewidth are the excited state lifetime ( $T_1$ ) and the pure dephasing time ( $T_2^*$ ). The excited state relaxation time is related to the natural linewidth ( $\Gamma_o$ ) by the simple relation

$$\Gamma_o = \frac{1}{2\pi c T_1}. \quad (2.6)$$

Unlike the excited state lifetime, the pure dephasing time results in broadening without a change in energy state of the LVM. This elastic scattering process causes a loss of phase coherence which occurs through interaction with bulk phonons of the crystal. At low temperatures the thermal motion of the phonons is “frozen” out and the natural linewidth is the dominant homogenous contribution. At higher temperatures the total homogeneous linewidth ( $\Gamma$ ) is then given by

$$\Gamma = \frac{1}{2\pi c T_1} + \frac{1}{\pi c T_2^*} \quad (2.7)$$

Homogenous processes are characterized by a Lorentzian spectral lineshape.

Inhomogeneous linewidth broadening can also occur due to high defect concentrations, strain fields, and various lattice defects. In such cases, the local environment will experience a random distribution of slightly different configurations causing the spectral line to contain more frequency components. Here, the spectral lineshape component is a Gaussian. Inhomogeneous broadening is especially dominant in amorphous or polycrystalline materials which contain a high degree of disorder to their crystal structure.

In special cases, the inhomogeneous contribution can be neglected and the IR linewidth

can be representative of the natural linewidth. This has been demonstrated in high quality Silicon crystals with low hydrogen concentration (1 ppm) [21]. At sufficiently low temperatures equation (2.6) allows experimental determination of the vibrational lifetime.

## 2.3 Vibrational Decay Mechanisms

The dynamics associated with vibrational excitation of hydrogen local modes involve many components. In addition to the local vibration between the oxygen and the hydrogen ion, the oxygen atoms, including the host, also undergo various thermal motions characterized by a phonon dispersion relation. Generally, any description of vibrational motion, transfer, or decay involving phonons will have a strong temperature dependence. This stems from the thermal population of phonon modes. At low temperatures, thermal lattice vibrations are minimized, and as the temperature is increased the phonon modes are gradually populated and the interaction phenomena become more pronounced. At the Debye temperature all the phonon modes are populated. This section outlines the theoretical framework for three important relaxation mechanisms for hydrogen LVMs: multiphonon decay, phonon-assisted proton tunneling, and phonon-assisted proton hopping.

### 2.3.1 Multiphonon Relaxation

When a localized molecular vibration in a solid relaxes (decays) by exciting bulk phonons in a single process, several phonons must be created simultaneously. This process is known as multiphonon relaxation [22]. The “order” of the decay process refers to the number of phonons involved in the LVM relaxation. Due to the commonality of this process in many physical systems, it is desirable to have a mathematical description

relating the lifetime temperature dependence to the phonons involved in the decay. It is also useful to define an energy gap as the difference between the highest phonon mode and the localized vibration. It has been found that the lifetime grows exponentially as this energy gap is increased. In other words, higher order processes are less efficient and therefore result in longer vibrational lifetimes.

### Mathematical Model

There are numerous theoretical approaches to multiphonon relaxation. A useful model, developed by Nitzan and co-workers, has been used successfully to describe relaxation of H modes in crystalline semiconductors [16] and could potentially apply to O-H related LVMs in the oxides. The essence of this theory is given here from Refs. [23], [24], and [25]. This model involves writing the Hamiltonian in the general form

$$H = \hbar\omega a^\dagger a + \sum_{\nu} \hbar\omega_{\nu} b_{\nu}^{\dagger} b_{\nu} + \sum_{\nu} (G_{\nu} B_{\nu} a^{\dagger} + G_{\nu}^* B_{\nu}^{\dagger} a), \quad (2.8)$$

where the (local) molecular oscillation has the creation and annihilation operators  $a$  and  $a^{\dagger}$  and oscillates at the frequency  $\omega$ . The medium is characterized by the set of bulk phonon frequencies  $\{\omega_{\nu}\}$  and the operators  $\{b_{\nu}\}$ ,  $\{b_{\nu}^{\dagger}\}$ , and the products  $B_{\nu} = \prod_{\nu} b_{\nu}$  and  $B_{\nu}^{\dagger} = \prod_{\nu} b_{\nu}^{\dagger}$ . The coupling between the molecule and the medium is represented by  $G_{\nu}$ .

Energy is conserved in the decay process so that the frequency of the molecular vibration is

$$\omega = \sum_{j=1}^N \omega_j^{\nu} \quad (2.9)$$

for an  $N$  phonon process.

The equations of motion for the molecular and medium states are first found in the

Heisenberg picture, and are simplified using the random phase approximation. It can be assumed the the medium states do not change appreciably during the decay process, which allows approximation of the medium Boson creation and annihilation operators by thermally averaged occupation number

$$\langle n_\nu \rangle_T = [\exp(\hbar\omega_\nu/k_B T) - 1]^{-1}, \quad (2.10)$$

where  $\langle \rangle_T$  represents the thermal average. Solving the equations of motion results in the definition of the vibrational relaxation width (i.e. inverse lifetime) given by

$$\gamma = \pi \sum_{\{\nu\}} |G_{\{\nu\}}|^2 n_{\{\nu\}} \rho_{\{\nu\}}, \quad (2.11)$$

where  $\rho_{\{\nu\}}$  is the compound many-phonon density of states.

For decay into  $N$  phonons, the temperature dependence of the lifetime stems from the thermally averaged commutator in equation (2.10). This results in the expression for  $n_{\{\nu\}}$  in equation (2.11) as

$$n_{\{\nu\}} = \frac{\exp(\hbar\omega/k_B T) - 1}{\prod_{\nu=1}^N [\exp(\hbar\omega_\nu/k_B T) - 1]}. \quad (2.12)$$

It is evident that a single phonon decay process is temperature independent. As the number of accepting phonons increases the temperature dependence becomes more pronounced. A characteristic multiphonon temperature dependence shows a broad plateau at low temperatures followed by a steep drop of in lifetime at higher temperatures as shown in Fig. 2.2.

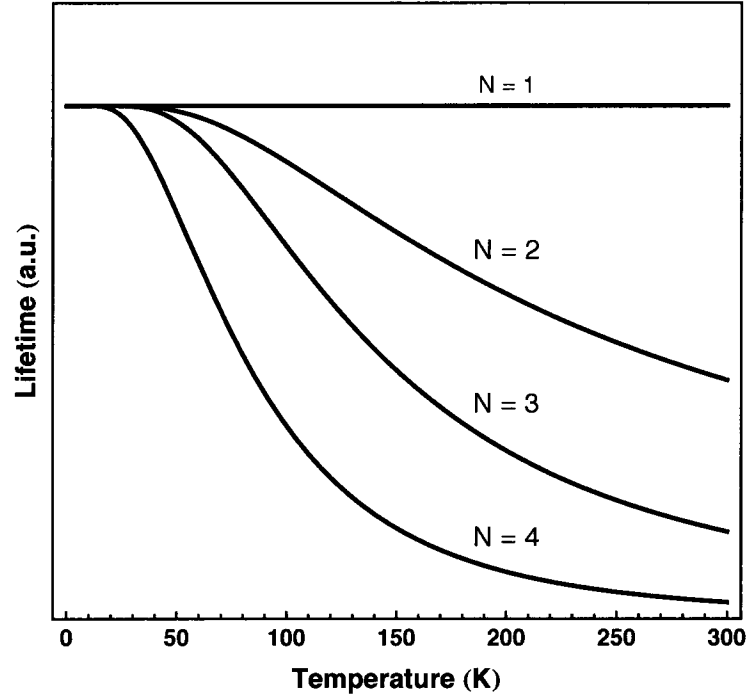


FIG. 2.2: Calculated lifetime temperature dependence for a decay into  $N$  phonons using Eq. (2.12).

### The “Frequency-Gap” Law

The vibrational relaxation rate in equation (2.11) includes many terms due to the large number of accepting channels. It is generally accepted that this sum can be reduced to a single term containing a dominant coupling coefficient,  $|G_{\{\nu\}}|^2$ . This assumption is based on the reduction of coupling strength with higher order decay processes. In other words, the dominant  $|G_{\{\nu\}}|^2$  term in the summation results from the accepting channel with the the smallest number of phonons that conserve energy according to equation (2.9). This simplifies the relaxation rate to

$$\gamma \simeq \pi |G_{\{\nu\}}|^2 n_{\{\nu\}} \rho_{\{\nu\}}, \quad (2.13)$$

A theoretical description of the coupling terms is lacking, however a qualitative description commonly used is  $G_\nu \simeq A\delta^N$ , where  $A$  is a constant and  $0 < \delta \ll 1$ . This relates the lifetime to the decay order and implies a frequency gap law for vibrational relaxation

$$\gamma \propto \delta^{2N}, \quad (2.14)$$

at constant temperature [25]. It is further shown in Ref. [24] that this frequency gap law can take the form of an exponential so that the vibrational lifetime may be expressed as

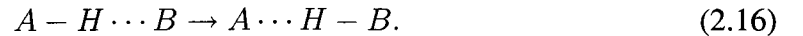
$$T_1 = A \exp(B N), \quad (2.15)$$

where  $A$  and  $B$  are constants related to the molecule-medium coupling and  $N$  is the order of the multiphonon decay process.

Equation (2.15) has been used to successfully describe the decay order of H and D wag modes in crystalline semiconductors (AlGa, GaAs, Ge, Si), which have been shown to decay by lowest order processes [16].

### 2.3.2 Proton Tunneling

Calculating the transition rate for the tunneling of a light atom through a potential barrier is a complex process. For protons in solids, tunneling occurs between two atomic hosts, A and B, and can be represented by the reaction process



There are many atomic vibrations involved and at low temperatures quantum effects must be accounted for properly. A relatively simple approach is to use the WKB (or adiabatic) approximation which describes the tunneling probability as having an exponential dependence on the integral of the classical momentum between turning points (equation (2.18)). The tunneling rate per unit time is then given as the attempt frequency ( $\nu$ ) times the probability of tunneling

$$k_{\text{tunnel}} = \nu \exp[-J(\mathbf{R})] \quad (2.17)$$

where

$$J(\mathbf{R}) = \frac{2}{\hbar} \int_a^b [2m(U(\mathbf{R}, r) - E(\mathbf{R}))]^{1/2} dr \quad (2.18)$$

is the tunnel integral describing the transparency of the potential barrier. Here  $a$  and  $b$  are the classical turning points,  $\mathbf{R}$  is the coordinate representing the reagent (A and B) spacing, and  $r$  is the position of the tunneling atom.  $U(\mathbf{R}, r)$  and  $E(\mathbf{R})$  are the potential and total energy of the tunneling atom and  $m$  is its mass. To include the effect of A and B vibrations (the lattice movement),  $J(\mathbf{R})$  can be expanded in powers of  $\mathbf{R}$

$$J(\mathbf{R}) = J(\mathbf{R}_o) + J'(\mathbf{R}_o)(\mathbf{R} - \mathbf{R}_o) + \frac{1}{2}J''(\mathbf{R}_o)(\mathbf{R} - \mathbf{R}_o)^2. \quad (2.19)$$

To fully describe the system, especially at low temperatures, both the local vibration and the vibrational motion of the surrounding atoms must be considered. The above approach only treats the LVM quantum mechanically.

The full quantum treatment, described in detail by Gol'Danskii et. al. in Ref [26] and by Trakhtenberg et. al. in Ref. [27], uses a double adiabatic approach and an expansion similar to equation (2.19). As mentioned above, the usual adiabatic technique divides the system into two subsystems, one being the rapid motion of the the electrons

and the other being the slower nuclear motion. This allows expressing the total wavefunction as a product of two wavefunctions. The double adiabatic approximation applies to systems where there is a further separation between fast and slow subsystems *within the nuclear motion*. In the case represented in equation (2.16) we have the fast intramolecular vibration (A-H) and the slow intermolecular vibration (A-B). The double adiabatic approximation applies when the mass of the transferred particle is much smaller than the host molecular mass or when the elasticity of the rapid subsystem is much greater than that of the slow intermolecular subsystem.

The rate constant using the double adiabatic approximation is found using a modified form of Fermi's Golden rule for radiationless transitions [26] [27]. The wavefunction for the system is written as

$$\Psi_{n,m,\nu}(\rho, \mathbf{r}, \mathbf{R}) = \psi_n(\rho, \mathbf{r}, \mathbf{R})\phi_{n,m}(\mathbf{r}, \mathbf{R})\chi_{n,m,\nu}(\mathbf{R}) \quad (2.20)$$

where  $n$ ,  $m$ ,  $\nu$  and  $\rho, \mathbf{r}, \mathbf{R}$  are the quantum numbers and position vectors for the electronic, intramolecular, and intermolecular subsystems, respectively. Denoting kinetic energy terms by the subscripts  $e$  and  $N$  for electronic and nuclear subsystems, the system Hamiltonian is then written as

$$H = T_e(\rho) + T_N(\mathbf{r}) + T_N(\mathbf{R}) + U(\rho, \mathbf{r}, \mathbf{R}). \quad (2.21)$$

The tunneling rate constant can then be found using

$$K = \frac{2\pi}{\hbar} A v_i \sum_f |\langle \chi_{n_f, m_f, \nu_f}(\mathbf{R}) | V_{n_f, m_f; n_i, m_i}(\mathbf{R}) | \chi_{n_i, m_i, \nu_i}(\mathbf{R}) \rangle|^2 \delta(E_f - E_i) \quad (2.22)$$

where  $\text{Av}_i$  denotes averaging over initial states and

$$V_{n_f, m_f; n_i, m_i}(\mathbf{R}) = \int \psi_{n_f} \phi_{n_f, m_f} H \phi_{n_i, m_i} \psi_{n_i}^* d\rho d\mathbf{x}. \quad (2.23)$$

The major mathematical task in determining the tunneling rate is to carry out this summation using the techniques of generating polynomials, operator calculus and the density matrix. This is done while incorporating the dependence of the intermolecular vibrations on the rapid subsystem. For the case of H tunneling between oxide ions, a one dimensional description using a single intermolecular ‘‘assisting’’ frequency has been successfully employed using the above approach [28] [29], and the rate equation for this somewhat simplified case is given by

$$K_{PT} = \nu \exp \left[ -J(R_o) + \frac{1}{8} \left( \frac{\partial J}{\partial R} \right)^2 (\delta_{O-O})^2 \coth(\hbar\Omega_o/4k_bT) \right]. \quad (2.24)$$

Similarly to equation (2.17),  $\nu$  is a frequency prefactor,  $\Omega_o$  is the frequency of the single assist mode,  $R_o$  is the equilibrium distance between neighboring oxygens, and  $\delta_{O-O}$  is the zero level amplitude of the O-O oscillation.  $J(R)$  is the tunneling integral given by equation (2.18).

This model is unique in that it takes into account the molecular vibrations of the host atoms surrounding the light mobile ion. This amounts to an assisting vibration and such process are referred to as vibration assisted. In the case of H tunneling in oxides, the A and B hosts in equation (2.16) represent O ions.

### 2.3.3 Proton Hopping

As with quantum tunneling, classical over-the-barrier hopping usually involves a strong coupling between the local O-H vibration and the bulk phonons. One theoretical approach that conveniently accounts for this coupling is that of the small polaron. A polaron is a quasiparticle consisting of a slowly moving charge in a medium surrounded by its accompanying polarization field. The polaronic picture is often employed to model transport and conductivity in systems with low mobilities – usually below  $1 \text{ cm}^2/\text{Vs}$  – where conduction is not band like [30]. The slowly moving charge can be a strongly phonon coupled electron or proton, and the inherent lattice coupling of polarons make them ideal to study phonon assisted proton hopping in solids.

Indeed, the polaron framework has been used to successfully model proton conduction by a number of researchers. Tomogose et. al. have used the small polaron model to calculate jump rates of interacting protons in metals [31] and more recently have applied this model to study proton conduction in  $\text{ABO}_3$  perovskites [32]. Here, activation energies for proton hops between minima of a double well potential were successfully calculated while accounting for coupling to the O–B–O bending mode. In a separate study by Fischer, the absorption spectra (including isotope effects) of O-H related modes in hydrogen bonded materials have been calculated by construction of a quasiparticle model similar to that of a small polaron [33]. Fischer further points out that three important requirements for implementation of the polaron model are (1) a double minimum potential well, (2) a strong coupling to the host lattice, and (3) a simple optical phonon spectrum. With this in mind, a study by Samgin presents a nice interpretation of proton migration in oxide based high temperature proton conductors. In this study a model for lattice-assisted proton migration was presented and successfully employed to calculate proton mobilities in

the perovskite  $\text{SrCe}_{1-x}\text{Yb}_x\text{O}_3$  [34].

The specific model used by Samgin for proton conduction in oxides is based on theoretical analysis of polaronic hopping in a H-bonded chain [35]. Theoretical details can also be found in Ref. [30]. The Hamiltonian for a proton polaron must contain three terms

$$H = H_{\text{proton}} + H_{\text{ph.}} + H_{\text{int.}} \quad (2.25)$$

which represent the proton, phonon, and proton-phonon interaction, respectively. Each component is written in terms of the creation (annihilation) operators  $a_m^\dagger$  ( $a_m$ ) for the proton and  $b_m^\dagger$  ( $b_m$ ) for the phonons as

$$H_{\text{proton}} = \sum_m \epsilon_m a_m^\dagger a_m \quad (2.26)$$

$$H_{\text{ph.}} = \sum_{\mathbf{q}} \hbar\omega_{\mathbf{q}} (b_{\mathbf{q}}^\dagger b_{\mathbf{q}} + 1/2) \quad (2.27)$$

$$H_{\text{int.}} = \sum_{\mathbf{q}, m} a_m^\dagger a_m \hbar\omega_{\mathbf{q}} [u_m(\mathbf{q}) b_{\mathbf{q}} + u_m^*(\mathbf{q}) b_{\mathbf{q}}^\dagger] \quad (2.28)$$

where  $\epsilon_m$  is the quasiparticle energy at lattice site  $m$ , the subscript  $\mathbf{q}$  indicates a particular phonon wavevector with frequency  $\omega_{\mathbf{q}}$ , and  $u_m(\mathbf{q})$  is a coupling term given by

$$u_m(\mathbf{q}) = \frac{1}{\sqrt{2N}} \gamma_m(\mathbf{q}) e^{-i\mathbf{q}\cdot\mathbf{R}_m}. \quad (2.29)$$

Here  $\gamma$  is a dimensionless coupling constant,  $\mathbf{R}_m$  is the position vector for the  $m^{\text{th}}$  lattice site, and  $N$  is the total number of sites. The above is treated by perturbation theory using

$$H' = \sum_{m \neq m'} J(\mathbf{R}_m, \mathbf{R}_{m'}) a_m^\dagger a_{m'} \quad (2.30)$$

a the perturbation Hamiltonian, which contains the weak resonance integral given by

$$J(\mathbf{R}_m, \mathbf{R}_{m'}) = \int \psi_{m'}^*(\mathbf{r} - \mathbf{R}_{m'}) H_{\text{proton}} \psi_m(\mathbf{r} - \mathbf{R}_m) d\mathbf{r}. \quad (2.31)$$

This represents the wavefunction overlap for protons at neighboring lattice sites and is responsible for charge transfer from site to site. Details of the transition rate calculation are given in Refs. [30] and [35]. By employing the density matrix (statistical operator) method, both the polaron current and mobility are determined. In the most simple case, an expression for the hopping mobility of a proton polaron is derived [34] as

$$\mu = \frac{\sqrt{\pi} q d^2 J^2}{2(k_b T)^{3/2} u \sqrt{\Omega}} \exp\left[-\frac{E_a}{k_b T}\right] \quad (2.32)$$

where  $q$  is the charge,  $d$  is the O-O distance,  $u$  is a coupling constant (proportional to  $\gamma$ ),  $\Omega$  is the phonon frequency, and  $E_a$  is the activation energy defined by

$$E_a = 2k_b T u^2 \tanh\left(\frac{\hbar\Omega}{4k_b T}\right). \quad (2.33)$$

Using the Einstein, relation the vibration-assisted hopping rate  $w_{m,m'}$  can be determined from the diffusion coefficient through

$$\mu = \frac{q}{k_b T} D = \frac{q}{k_b T} d^2 w_{m,m'}. \quad (2.34)$$

For low frequency assist phonons,  $\hbar\Omega \approx k_b T$  at temperatures close to 300 K, and the hopping time (inverse hopping rate) can be approximated as

$$\tau = \frac{1}{w_{m,m'}} = A u \Omega \exp[2u^2 \tanh(\hbar\Omega/k_b T)] \quad (2.35)$$

where  $A$  (in units of time squared) is fitting parameter which contains the resonance integral  $J$ . In determining the assist phonon from temperature dependent lifetime data, note that the dominant contribution comes from the exponent and the pre-exponential parameters resemble a frequency pre-factor similar Arrhenius type diffusion.

# CHAPTER 3

## Experimental Details

This chapter presents an overview of the equipment and techniques necessary for hydrogen defect characterization and vibrational lifetime measurements. The two primary experimental techniques, FTIR absorption spectroscopy and picosecond pump-probe spectroscopy, are particularly well suited to characterize O-H modes in oxides. The former provides frequency domain information and can be used to quantify atomic configuration, vibrational frequencies, and defect concentration while the later yields direct time domain measurements of vibrational lifetimes. The general approach when investigating the microscopic nature of H in oxides is to first identify and characterize the vibrational frequencies of the O-H related absorption lines. This includes identifying isotope lines (if available) and studying the temperature dependence of both the fundamental vibrational frequency and the infrared linewidth. Once fully characterized, the dynamics of the local mode are then studied by the pump-probe technique. Here, the lifetime temperature dependence and isotope effect provide valuable information on the LVM–host coupling and the local mode decay process.

### 3.1 Fourier Transform Infrared Absorption Spectroscopy

Since the development of computational fast Fourier transforms, the Fourier Transform Infrared Spectrometer (FTIR) has become a standard tool for materials characterization. It can be used to identify samples or quantify the concentration of particular components in a material and is ideal for studying hydrogen defects in solids since the absorption lines associated with the stretch modes are well above the crystal's phonon band.

In a FTIR spectrometer light from a broad band blackbody source is passed through a standard interferometer. The two output beams are then sent through the sample and an interferogram is recorded as the delay between beams is varied. A computer then takes the Fourier Transform to convert the time domain signal into the frequency domain which reveals the absorption spectra of the sample. A basic schematic of a standard FTIR interferometer is shown in Fig. 3.1.

Mathematically, the intensity of the interferogram as a function of optical path difference between the two beams ( $\delta$ ) can be written as

$$I'(\delta) = \frac{1}{2}I(\nu)(1 + \cos(2\pi\nu\delta)). \quad (3.1)$$

This comes from taking the absolute value squared of the electric fields of the two beams. The first term is a dc component and is usually neglected because the cosine term contains all the spectroscopic information. In reality instrumental limitations such as beamsplitter efficiency and detector response impose a frequency dependent proportionality factor,  $B(\nu) \propto I(\nu)$ , on the signal, so that the interferogram can be expressed simply as

$$S(\delta) = B(\nu)\cos(2\pi\nu\delta). \quad (3.2)$$

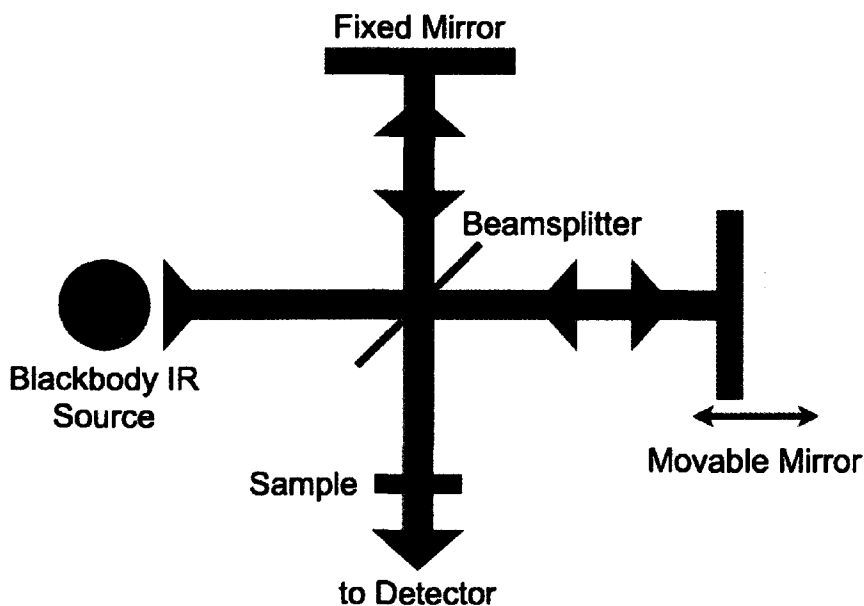


FIG. 3.1: A Michelson-Morley interferometer for FTIR spectroscopy.

For a broadband light source, this expression is integrated over all frequencies to give

$$S(\delta) = \int_{-\infty}^{+\infty} B(\nu) \cos(2\pi\nu\delta) d\nu. \quad (3.3)$$

The above expression represents the signal at the detector and is half of a Fourier Cosine Transform pair. The absorption spectrum of interest,  $B(\nu)$ , is then found computationally by performing the inverse transform given by

$$B(\nu) = 2 \int_0^{+\infty} S(\delta) \cos(2\pi\nu\delta) d\delta. \quad (3.4)$$

If the optical path difference,  $\delta$ , is measured in cm, then the absorption spectra will be in inverse units  $\text{cm}^{-1}$  or wavenumbers [36].

This relatively simple method is advantageous over techniques which employ a grat-

ing (such as a scanning monochromator), because all the spectroscopic information (full wavelength range) is collected in a single measurement. Each measurement usually takes less than one second, which allows for averaging of many scans to achieve accurate low noise data in a short period of time.

For a standard FTIR measurement, a background scan is first collected to record any absorption from the atmosphere of the sample chamber. Next, the sample is inserted into the beam path and another scan is collected. Any difference between these two measurements will be due to the absorbance of light by the sample. Data can be analyzed as % Transmission or Absorbance. % Transmission is defined as the ratio of the transmitted intensity ( $I_t$ ) to the incident intensity ( $I_o$ ) on the sample. Absorbance is defined as  $A = -\text{Log}(I_t/I_o) = -\text{Log}(\%T)$ .

From the absorbance, the absorption coefficient is defined as

$$\alpha = \text{Ln}(10)(A/x) \quad (3.5)$$

where  $x$  is the thickness of the sample. The concentration of absorbing species is then related to the integrated absorption coefficient by

$$N = C \int \alpha d\nu \quad (3.6)$$

where  $\nu$  is the frequency in wavenumbers and the integration is over the baseline corrected IR peak of interest. To provide an accurate estimate of the number of absorbing dipoles, the constant  $C$  must be found from calibration experiments.

As an example, an FTIR spectra in Fig. 3.2 shows the spectroscopic signatures of the O-H (a) and O-D (b) stretch modes in  $\text{TiO}_2$ . The vibrational frequencies are well above

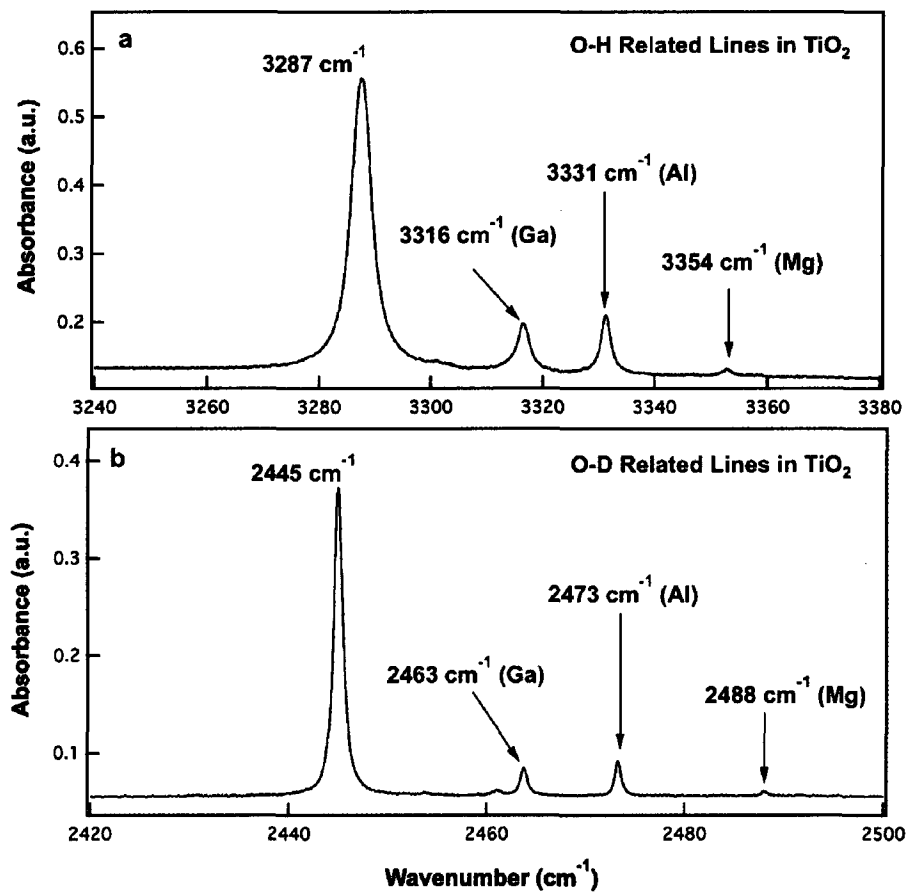


FIG. 3.2: Hydrogen and deuterium related stretch modes in rutile TiO<sub>2</sub> identified by FTIR absorbance spectroscopy at 10K.

the highest bulk phonon absorption around 850 cm<sup>-1</sup>. The high energy sidebands have been identified by Johnson and co-workers as O-H (O-D) stretch modes associated with a nearby impurities in the crystal lattice [37] as indicated in the inset.

## 3.2 Laser System and Vibrational Lifetime Measurements

Local vibrational modes are often characterized by their infrared absorption linewidths measured by traditional FTIR spectroscopy described in the introduction. For example, hydrogen related modes in crystalline solids are often identified by having a vibrational frequency comparable to that of a free O-H molecule (around  $3,500\text{ cm}^{-1}$ ). However, conventional vibrational spectroscopy does not provide direct information on the dynamics (i.e. vibrational decay). Pump-probe infrared spectroscopy, a.k.a transient bleaching spectroscopy, provides this time resolution we require to explore the dynamical behavior and coupling mechanisms of hydrogen local modes.

### 3.2.1 Laser System

The transient bleaching technique requires tunable, infrared picosecond laser pulses. These are achieved using a high power Ti:Sapphire laser system to seed an optical parametric amplifier (OPA). The amplifier laser system consists of both regenerative (REGEN) and a two-pass amplification stages. The large number of passes through the cavity in the REGEN allows for high gain and stable output. In order to maintain sufficient output power from the amplifier, one should periodically check that the seed and pump beams are properly coupled into the REGEN. The cavity itself should be stable once aligned properly and output beam steering is independent of any drift of the seed or pump beams. This stability is critical for operation of the OPA which operates on nonlinear optical principles. A schematic of the laser setup on the optics table is illustrated in Figure 3.3. More details about the amplifier and OPA can be found in Appendix A.

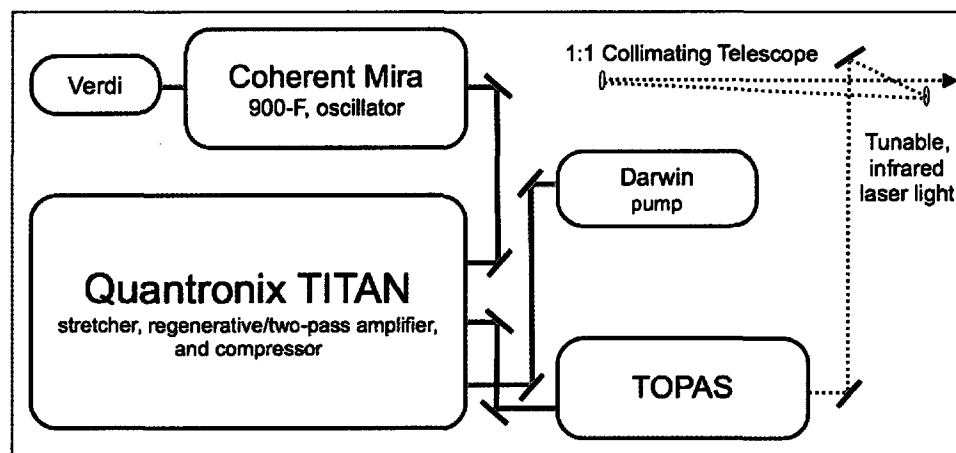


FIG. 3.3: Top-down schematic of the picosecond laser system used in this work.

### 3.2.2 Measuring Vibrational Lifetimes

A schematic of the pump-probe setup used for this work is shown in Figure 3.4. The output beam from the OPA (Quantronix TOPAS) is first collimated by a pair of curved mirrors and sent through a pair of irises placed about two meters apart. The alignment of the infrared beam is challenging, therefore it is crucial to use a Helium-Neon (HeNe) alignment laser directed through these same two initial irises. The initial setup and alignment are done with the HeNe, and then as long as the infrared beam passes through the initial irises the beam paths should be the same.

The infrared beam is split into a probe (10% intensity) and a pump (90%). The probe passes through a motorized delay stage and then the two beams are focused by a parabolic mirror on the sample. When the pump is incident on the sample it will excite a portion of the hydrogen defects to their first vibrational state. The sample is then said to be “bleached,” because due to the population of this excited state, the transmission coefficient of the sample is increased. The transmitted intensity of the probe beam will

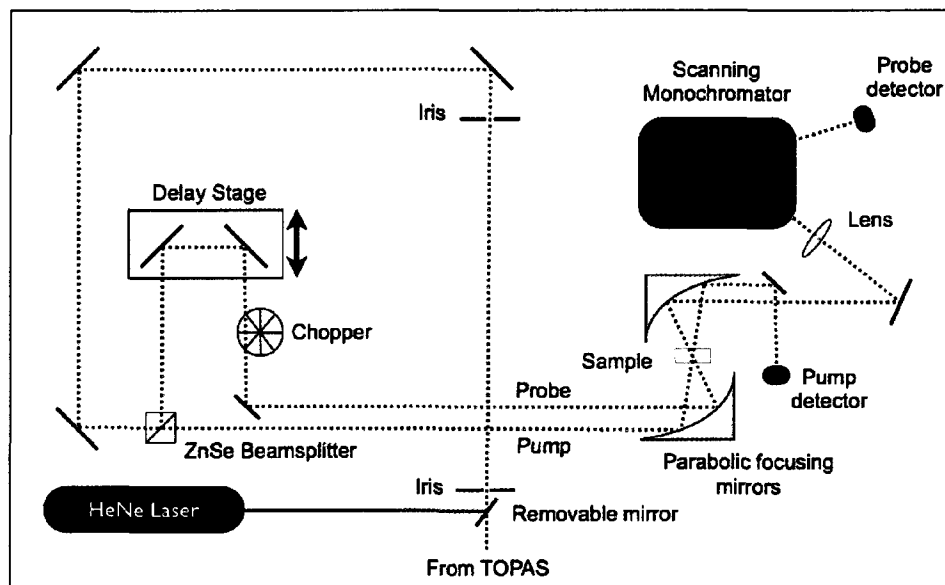


FIG. 3.4: Schematic of experimental pump-probe setup used in this work. The laser system is the Quantronix TOPAS described earlier.

then be proportional to the excited state population. Detection of the probe beam as a function of the delay between pulses then gives a direct time-domain measurement of the vibrational decay of this excited state. The pump beam is modulated at approximately 310 Hz with an optical chopper and a lock-in amplifier is used to detect probe light that has the same modulation frequency and phase as the pump.

It is very important that the two beams overlap both spatially and temporally on the sample. In order to check spatial overlap, a  $25 \mu\text{m}$  pinhole can be placed at the focus and the pump and probe can be adjusted to pass through it cleanly. To find the zero time overlap of the two beams it is helpful to use a sample that will give a strong nonlinear response such as a piece of Germanium, which has a strong two-photon absorption signal at a wavelength of  $3 \mu\text{m}$  as shown in Figure 3.5.

Once the setup is aligned, the Germanium reference sample is replaced with the

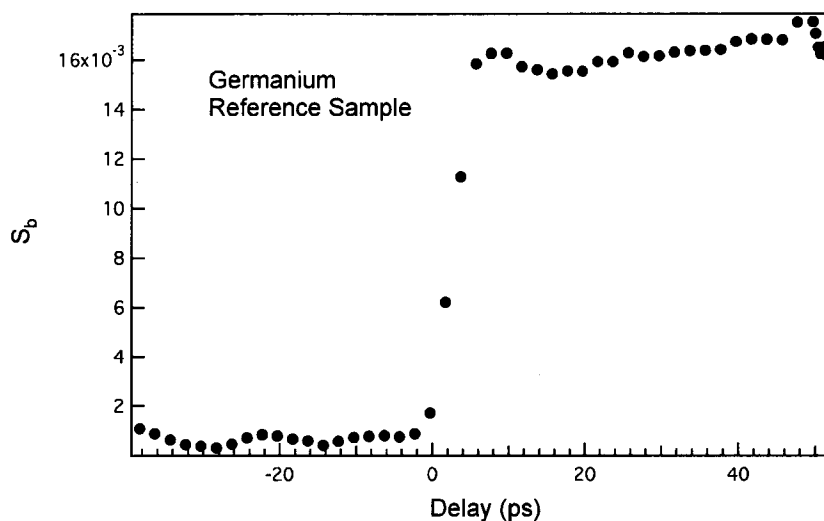


FIG. 3.5: Two photon signal from a Ge reference sample used to find the temporal overlap of the pump and probe beams.

cryostat containing the sample of interest. The OPA must be tuned to the correct frequency to be resonant with the O-H (or O-D) stretch mode. In order to check this, the spectrum of the probe beam passing through the sample is measured with the scanning monochromator (McPherson 218, with a 300 gr/mm grating blazed at 3,000 nm). The resonance condition is indicated by a dip in the spectrum corresponding to the absorption of the O-H (O-D) in the material. An example of the probe beam passing through a deuterated  $\text{KTaO}_3$  sample is shown in Figure 3.6. The monochromator is then used to match the detecting wavelength with the dip in the figure.

Now that the spatial and temporal overlap are optimized and resonant excitation condition achieved, one can measure the vibrational lifetime by scanning the delay between pump and probe beams. In order to maximize the pump-probe signal, it is often necessary to adjust the position of the sample to make sure it is perfectly in the focus of the two beams. Once optimized at 80K, liquid helium can then be used to cool to 10K and one can

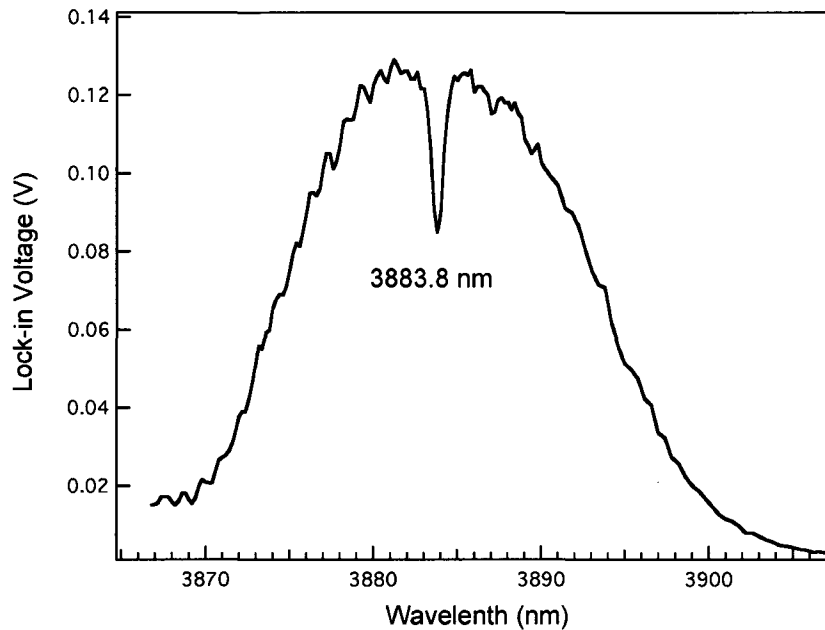


FIG. 3.6: Probe spectrum passing through  $\text{KTaO}_3$  at 80k. Dip at 3883.8 nm ( $2575 \text{ cm}^{-1}$ ) corresponds to the O-D stretch mode.

begin to measure the temperature dependence of the lifetime. It is important to keep in mind that in most materials the vibrational frequency will shift with temperature, so it is often necessary to readjust both the TOPAS and detection (monochromator) wavelength settings.

### 3.3 Materials

As motivated in section 1.1, there has been considerable focus on understanding the basic properties of hydrogen impurities in oxide materials. Hydrogen is an omnipresent impurity in many as-grown oxide crystals and can significantly impact the electronic, structural, and optical properties of these crystals for practical device applications [1] [38] [39] [40]. Generally, the dynamics and diffusion of hydrogen ions in oxides depends

largely on the crystal structure of a particular material, so it is important to choose materials that are interesting, both technologically and scientifically, and show diverse structural properties.

One very important class of oxide crystals is the cubic perovskite structure. Many perovskites exhibit ferroelectric properties and interesting phase transitions. Additionally, many have been found to be proton conducting at elevated temperatures and are technologically interesting for a number of hydrogen related alternative energy applications. Iwahara and co-workers have even demonstrated fuel cells based on these oxides [41]. Potassium tantalate or  $\text{KTaO}_3$  is a widely studied material because it is an established proton conductor [42] and, unlike other perovskites, it retains the cubic structure at temperatures as low as a few Kelvin [43].

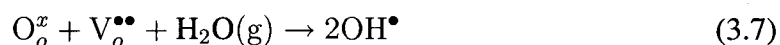
The equilibrium position of the proton in  $\text{KTaO}_3$  is between two  $\text{O}^{2-}$  ions along the edge of the oxygen octahedra – a characteristic of the perovskite structure. Proton diffusion or conduction is isotropic and consists of sequential hops between and reorientations around oxygen ions to which the proton bonds – a process known as the Grotthuss mechanism [9].

Another widely studied and important material is titanium dioxide or  $\text{TiO}_2$ . This oxide has seen much recent interest as a promising photo-anode for water splitting from sunlight in which surface reactions with hydrogen are very important [6] [7]. The rutile crystal structure contains spatially open channels along the  $c$  direction which allow for significantly higher proton mobility along this axis. This means that, in contrast to  $\text{KTaO}_3$ , proton diffusion in  $\text{TiO}_2$  is anisotropic. Such open channels are also found in other oxides such as quartz. In equilibrium the O-H bond is oriented so that the proton occupies a portion of the open channel and migration consists of jumps between  $\text{O}^{2-}$  ions along the channel walls [44]. Here, reorientations of the O-H bond are not needed, thus studying  $c$

axis diffusion in rutile is selective for only one migration mechanism.

### 3.3.1 Sample Preparation

There are various treatments to incorporate hydrogen ions into single crystal oxides. All treatments involve heating samples in a hydrogen containing atmosphere. One common method is to seal the sample in a quartz ampule that has been evacuated and backfilled with H<sub>2</sub> gas and anneal it at high temperature, usually above 500°C. The treatments used for this work, however, involve annealing in flowing water (or heavy water) vapor in a tube furnace. When single crystal oxides are heated in a water environment, the following reaction takes place on the surface to introduce H or D into the bulk



using Kröger-Vink notation [45]. Here the oxygen vacancies ( $V_o^{\bullet\bullet}$ ) react with the water vapor to introduce protons into the lattice. This notation indicates that the protons are bound to a  $O^{2-}$  ion to form a substitutional  $OH^-$  ion. The proton is then free to migrate (hop or tunnel) between oxygen ions and permeate the lattice.

#### Potassium Tantalate, $KTaO_3$

Single crystal samples  $KTaO_3$  were grown by a spontaneous nucleation technique first described by Hannon [43]. This involves placing 20 g of  $Ta_2O_5$ , 9.2 g of  $K_2CO_3$ , and  $\sim \frac{1}{2}$  g of  $TiO_2$  on a platinum crucible and holding the mixture at 1450°C for 1-2 hours. The temperature of the crucible is then lowered in increments of 20°C per hour. This technique produces single crystals of about 0.5 cm on a side. Crystal growth was performed at at Oak Ridge National Laboratory by Dr. Lynn A. Boatner (Materials Science

and Technology Division). Due to the growth environment (atmosphere) these crystals contain a large initial concentration of hydrogen. To increase the concentration to approximately  $10^{17} \text{ cm}^{-3}$ , samples were annealed in water vapor for one hour at  $1050^\circ\text{C}$ . Deuterated samples were prepared by first annealing in vacuum then in  $\text{D}_2\text{O}$  vapor for 4 hours also at  $1050^\circ\text{C}$ .

### **Rutile Titanium Dioxide, $\text{TiO}_2$**

The rutile  $\text{TiO}_2$  single crystal samples used in this work were grown by the flame fusion, or Verneuil, method. This crucible-free growth method involves the mixing of a titania starting powder with oxygen and hydrogen carrier gasses. Combustion of these two gasses at around  $2000^\circ\text{C}$  causes the powder to melt and slowly form a single crystal boule [46]. Typical samples on the order of  $10 \times 10 \times 1 \text{ mm}^3$  are cut from the single crystal boule and chemically polished on the large surfaces. These samples also contain a high as-grown hydrogen concentration due to the hydrogen carrier gas. As with  $\text{KTaO}_3$ , hydrogen can be further incorporated into the sample by annealing at  $1050^\circ\text{C}$  in a flowing  $\text{H}_2\text{O}$  environment. For deuterated samples, similar anneals are performed with  $\text{D}_2\text{O}$  vapor. Concentrations on the order of  $10^{17}$  to  $10^{18}$  per  $\text{cm}^3$  can be achieved with annealing times of one hour for hydrogen and 4 hours for deuterium. For this work, rutile samples were obtained from Oak Ridge National Lab and Commercial Crystal Laboratories (Naples, FL).

## CHAPTER 4

# Proton Tunneling in $\text{KTaO}_3$

Quantum tunneling of protons is a universal phenomenon commonly seen a wide variety of physical [47] and biochemical process [48]. Oxides such as  $\text{KTaO}_3$  are often considered proton conductors at sufficiently high temperatures and it is generally accepted that proton tunneling can contribute to migration at lower temperatures. Proton migration is attributed to the Grotthuss mechanism [9], consisting of sequential O-H...O transfer and O-H reorientation steps [8]. Theoretical studies have addressed the preferred sites, transition states, barrier heights, and conduction pathways in these oxides using a first principles [11] or a molecular dynamics approach [8]. However, none of these takes directly into account the vibrational dynamics and relaxation mechanisms of the O-H complex, which can considerably affect the proton diffusion rate. Thus, the focus of this chapter is to explore the relationship between vibrational excitation and proton tunneling in potassium tantalate ( $\text{KTaO}_3$ ).

## 4.1 Proton Tunneling: a Vibrational Decay Channel

$\text{KTaO}_3$  is an ideal system to investigate the interplay between O-H vibrational dynamics and proton tunneling since the associated stretch mode can be excited cleanly and is well separated in energy from the phonon bath. Additionally,  $\text{KTaO}_3$  and other perovskite-structured oxides exhibit significant proton conductivity at elevated temperatures [49] and quantum tunneling has been suggested both experimentally [50] and theoretically [11] at sufficiently low temperatures.

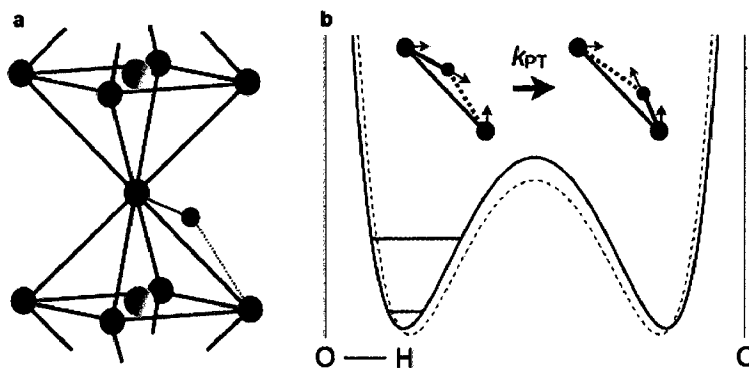


FIG. 4.1: The ionic configuration around the proton in a perovskite lattice. (a) The proton moves throughout the oxygen octahedral network. (b) the potential energy diagram of the hydrogen atom, tunneling from one well to another. The vibrational ground and first excited state are shown in the left-hand well of the DMP. The inset indicates the vibrational modes associated with phonon-assisted tunneling.

Figure 4.1 depicts the perovskite sublattice of  $\text{KTaO}_3$ . The interstitial H or D ion is bonded to an oxide ion with the O-H axis oriented along the bisector of the two oxygen nearest neighbors. The proton forms a weak hydrogen bond with the second-nearest neighbor oxygen and thus occupies a double Morse-type potential well, as shown on the right hand side. The infrared absorption spectra of the O-H and O-D stretch modes are shown in Fig. 4.2, where the narrow linewidths ( $\Delta\omega$ ) indicate a weak coupling to the

surrounding lattice.

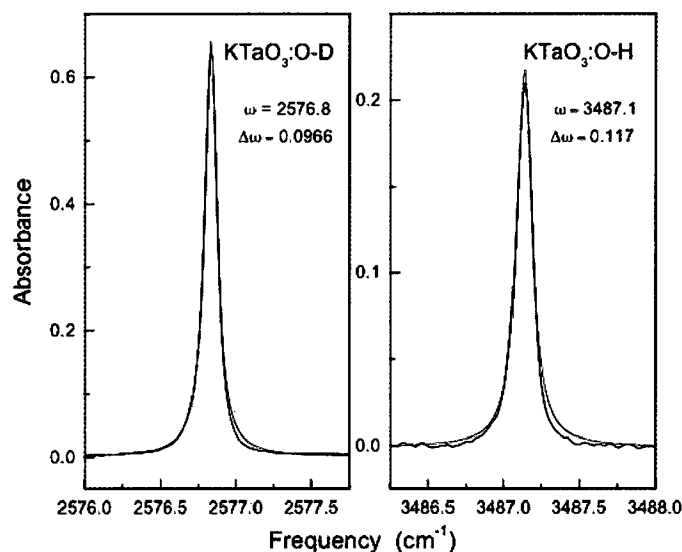


FIG. 4.2: The O-H and O-D stretch modes in KTaO<sub>3</sub> identified by FTIR. Fits to a Lorentzian lineshape give linewidths shown in the inset.

Quantum mechanical tunneling of protons in oxides usually occurs along the direction of this hydrogen bond bridge [51]. The strong dependence of the tunneling rate on O-O distance, i.e., barrier width, creates two interesting scenarios. First, excitation to higher vibrational levels may lead to an increased tunneling rate because the barrier effectively “narrows” as the proton moves up in energy from the bottom of the potential well. Second, large-amplitude conformational motions can bring the oxide ions in close proximity (indicated by the dashed line in Fig. 4.1), also promoting tunneling. While the latter leads to a temperature dependent transfer rate and is termed “vibration-assisted tunneling,” the former strongly competes with multiphonon decay processes and may be effective even at elevated temperatures. Thus, excited state proton tunneling is an effec-

tive decay channel for the O-H stretch mode.

## 4.2 Vibrational Lifetimes and Reverse Isotope Effect

The vibrational lifetimes in  $\text{KTaO}_3$  are measured by the transient bleaching technique described in Chapter 2. The O-H and O-D stretch modes exhibit unusually long lifetimes  $T_1 = 101 \pm 3\text{ps}$  (at 70 K) and  $405 \pm 5\text{ps}$  (at 100 K), respectively, shown in Fig. 4.3. The later represents the longest vibrational lifetime so far reported for a hydrogen related mode in a crystalline solid [52]. This observation for an interstitial hydrogen defect is surprising considering that long lifetimes have only been previously observed for vacancy related complexes in the covalent semiconductors Si and Ge. In such vacancy defects the open lattice structure promotes weak coupling to bulk lattice vibrations resulting on longer lifetimes.

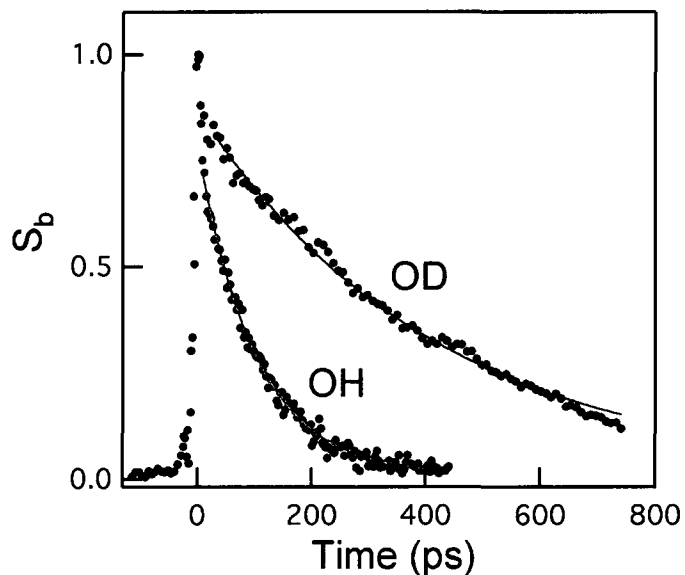


FIG. 4.3: Transient bleaching signal,  $S_b$  of the O-H and O-D stretch modes in  $\text{KTaO}_3$

For hydrogen local mode relaxation into phonons, the “frequency-gap law” predicts that the vibrational lifetime depends on the decay order, or the number of phonons involved [16]. This implies that a lower frequency mode will have a shorter lifetime because it is closer to the highest phonon frequency. Thus, the large reverse isotope effect shown in Fig. 4.3 is unexpected and, therefore, inconsistent with the vibrational decay being due to the excitation of bulk phonons.

The next most likely candidate for a vibrational decay channel is the wag mode, which is also a localized vibration with a frequency well above the bulk phonon spectrum. For this work, the O-H wag mode has been identified through a careful series of high-resolution infrared absorption measurements, shown in Fig. 4.4, performed by Ms. Lanlin Wen and Prof. Michael Stavola at Lehigh University. A hydrogenated  $\text{KTaO}_3$  sample was annealed at temperatures ranging from 700 to 950°C and the intensity of the absorption peaks of the stretch and combination modes were observed to decay as hydrogen was annealed out of the sample. A peak at  $1058\text{ cm}^{-1}$ , corresponding to roughly the difference between the stretch and combination mode frequencies was monitored and observed to decay with the known O-H related modes, thus establishing the O-H wag mode frequency. For the O-D wag mode, a frequency of approximately  $755\text{ cm}^{-1}$  is estimated based on the reported combination mode and the inclusion of a small anharmonic shift [53].

Since excited local vibrational modes couple much stronger to other localized modes [15], it is most likely that the O-H and O-D decay channels constitute three wag modes

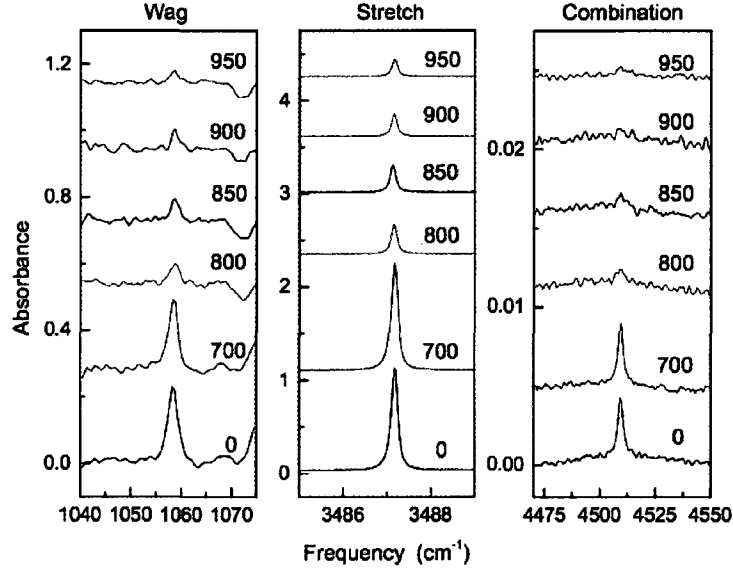


FIG. 4.4: FTIR spectra taken after consecutive anneals at elevated temperatures (degrees Celsius) identifying the O-H wag mode.

and one bulk phonon at  $\sim 312 \text{ cm}^{-1}$ . Explicitly, this can be written as

$$\omega_{LVM} = 3 \times \omega_{\text{wag}} + \omega_{\text{phonon}} \quad (4.1)$$

$$\omega_{OH}(3487 \text{ cm}^{-1}) = 3 \times 1058 \text{ cm}^{-1} + 313 \text{ cm}^{-1} \quad (4.2)$$

$$\omega_{OH}(2577 \text{ cm}^{-1}) = 3 \times 755 \text{ cm}^{-1} + 312 \text{ cm}^{-1} \quad (4.3)$$

where (4.1) is a general statement of energy conservation between local and accepting modes. It is reasonable that the involvement of a high number of accepting modes as well as the weak coupling to the wag mode is responsible for the long lifetimes of the O-H and O-D stretch modes in  $\text{KTaO}_3$ . The long lifetime seems to be quite common in other perovskite oxides in which the associated stretch mode shows consistently narrow linewidths, e.g. in  $\text{SrTiO}_3$  [54] and  $\text{LiNbO}_3$  [55]. Indeed, the lifetime of the O-H stretch

mode in  $\text{SrTiO}_3$  ( $3514 \text{ cm}^{-1}$ ) was measured in this work to be  $112.8 \pm 6 \text{ ps}$  at 80K. It is important to note, however, that the measured O-H (O-D) IR linewidth of 0.12 (0.097)  $\text{cm}^{-1}$  observed here is not representative of the vibrational lifetime according to (equation xx, linewidth relation). These linewidths are measured at 4 K with an instrument resolution of  $0.03 \text{ cm}^{-1}$  indicating that the inconsistency is most likely due to inhomogenous broadening mechanisms such as strain fields from crystalline impurities. This indicates that, unlike some high purity crystalline semiconductors such as Si and Ge, the vibrational lifetimes cannot be determined from infrared absorption measurements.

The above analysis indicates that both the O-H and O-D stretch modes have essentially the same multiphonon decay channel: three wag modes and a residual phonon. Therefore, one can expect both modes to have a very similar multiphonon decay rate. The central question then becomes, what is the additional mechanism responsible for the different decay rate of the O-H mode?

### 4.3 Lifetime Temperature Dependence

To address this issue, important information about the decay mechanism of the local modes is obtained from the temperature dependence of the vibrational lifetime, shown in Fig. 4.5. The lifetime of the O-H stretch mode exhibits a rather unusual temperature dependence: it decreases almost immediately at low temperatures with a gentle slope. In contrast, the O-D curve is very typical of a multiphonon decay process. It shows a broad plateau at low temperatures followed by a rapid decrease in lifetime which is due to the thermal population of phonons. Moreover, the large reverse isotope is most dominant at low temperatures. This clearly indicates that the decay mechanisms for the two isotopes are different. Since the multiphonon contributions to the decay have been determined to

be the same, there must be an additional mechanism responsible for the shorter lifetime of the O-H stretch mode.

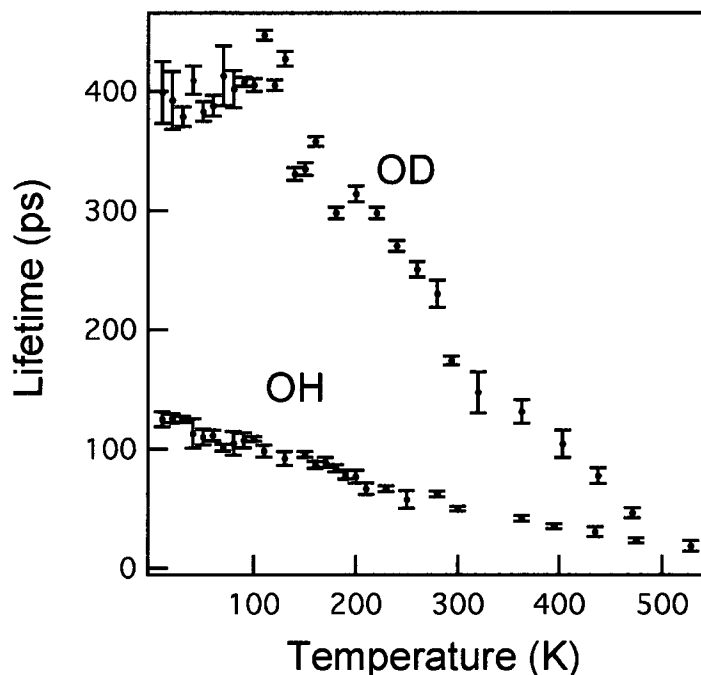


FIG. 4.5: Temperature dependence of the O-H and O-D stretch mode lifetimes

This additional decay mechanism can be logically attributed to an excited state proton transfer process. As with any transfer motion between oxygen ions, the proton can either hop over or tunnel through the potential energy barrier. Both process would yield a reverse isotope effect because the lower zero point energy of the O-D mode makes it less likely to leave the host configuration (hence a longer lifetime). Furthermore, classical hopping would require an activation energy of 0.89 eV and such a thermally activated process would vanish at low temperatures [45]. This requirement is inconsistent with the data shown in Fig. 4.5. Hence, the additional decay mechanism is attributed to proton tunneling. The tunneling rate for deuterium is estimated to be negligible, therefore the

multiphonon decay rate can be expressed as  $1/T_1$  for the O-D stretch mode. Since the multiphonon contributions are approximately the same for both isotopes we can express the experimental proton tunneling rate ( $k_{PT}$ ) as the difference between the O-H and O-D decay rates (inverse lifetimes). This is represented as

$$\frac{1}{T_{1(OH)}} = \frac{1}{T_{1(OD)}} + k_{PT} \quad (4.4)$$

$$k_{PT} = \frac{1}{T_{1(OH)}} - \frac{1}{T_{1(OD)}}. \quad (4.5)$$

Figure 4.6 shows the experimental proton-tunneling rate  $k_{PT}$  as a function of inverse temperature. The tunneling rate at room temperature is about  $(70 \text{ ps})^{-1}$ , while at room temperature it is  $(135 \text{ ps})^{-1}$ . At lower temperatures,  $k_{PT}$  is almost temperature independent. It is interesting to note that the tunneling rate between O-H ground states in the similar perovskite oxide  $\text{BaCeO}_3$  is  $10^3 \text{ s}^{-1}$  at room temperature, while from the first excited state in  $\text{KTaO}_3$  it is  $10^{10} \text{ s}^{-1}$ , representing an increase in 7 orders of magnitude.

## 4.4 Phonon-Assisted Proton Tunneling

It is important to note that the temperature dependence of the tunneling rate indicates the involvement of bulk phonons in the transfer process. The solid red line in Fig. 4.6 shows an excellent fit of  $k_{PT}$  to the expression derived by Trakhtenberg and co-workers (equation (2.24) in Chapter 2) shown again below.<sup>1</sup> Recall that this model incorporates

<sup>1</sup>Acceptable values for the frequency pre-factor,  $\nu$ , are in the range  $10^{13} < \nu < 10^{14} \text{ s}^{-1}$ . Here  $\nu = 5 \times 10^{13} \text{ s}^{-1}$ . The other fit parameters for the experimental proton transfer rate are  $J(R_o) = 3.481 \pm 0.075$  and  $1/8(\partial J/\partial R)^2(\delta_{O-O})^2 = 0.3043 \pm 0.0873$ .

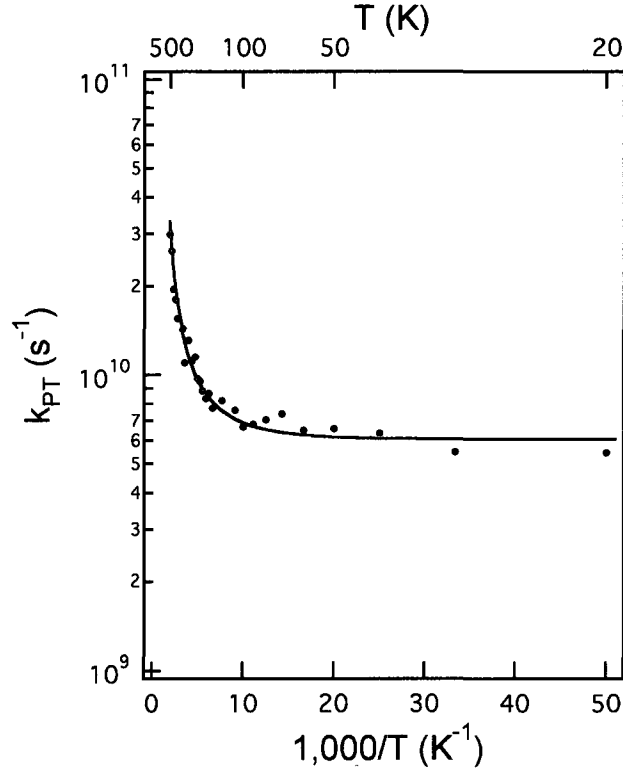


FIG. 4.6: Experimental proton tunneling rate,  $k_{PT}$ , extracted from the vibrational lifetimes of the O-H and O-D stretch modes. The solid line is a fit to Trakhtenberg's model.

the potential energy in the tunneling integral  $J(R)$ .

$$K_{PT} = \nu \exp \left[ -J(R_o) + \frac{1}{8} \left( \frac{\partial J}{\partial R} \right)^2 (\delta_{O-O})^2 \coth(\hbar\Omega_o/4k_bT) \right].$$

Here,  $\nu$  is a frequency prefactor,  $\Omega_o$  is the frequency of the assist mode,  $R_o$  is the equilibrium distance between neighboring oxygens, and  $\delta_{O-O}$  is the zero level amplitude of the O-O oscillation.  $J(R)$  is the tunneling integral given by equation (2.18). For hydrogen in  $\text{KTaO}_3$  the O-O separation distance is  $2.81 \text{ \AA}$  and the barrier height for the double Morse potential is  $0.9 \text{ eV}$ . The frequency of the assist mode,  $\Omega_o$ , is found to be  $228 \pm 51 \text{ cm}^{-1}$ ,

which is in good agreement with the  $200 \text{ cm}^{-1}$  value of the  $\Gamma_{15}$  optical phonon corresponding to a O-Ta-O bending motion [56] [57].

The observation of phonon-assisted tunneling is further supported by the fact that the decay of the O-H stretch mode is associated with this process. Because the LVM does not remain in the excited state, the population relaxation is indicative of an incoherent tunneling process where the interaction with the phonon bath leads to dephasing of the stretch mode [51]. High resolution infrared absorption spectra of the O-H and O-D stretch modes do not exhibit proton or deuteron tunnel splitting and, thus, give no evidence for coherent tunneling. Even below 70 K where  $k_{PT}$  is weakly temperature dependent, the self-trapping distortion of the potential energy surface localizes the light interstitial at a specific lattice site and, because neighboring sites are inequivalent, most likely prevents coherent tunneling.

As mentioned earlier, tunneling is an important component of proton conduction, so it is reasonable to expect that the long lifetimes (i.e. low multiphonon decay rates) play a role in the high proton conductivities commonly observed in many perovskite oxides. As evident in Fig. 4.1b, vibrational excitation effectively lowers the energy needed to promote the proton from one oxygen host to another. Qualitatively speaking, prolonged occupation of this upper state increases the probability for transfer - either by tunneling at low temperatures or by thermally activated hopping at elevated temperatures (usually above  $500^\circ\text{C}$ ). This assertion is supported by the truncated harmonic oscillator model for hydrogen desorption, in which a large  $T_1$  can yield a high hydrogen dissociation rate [58].

Trakhtenberg's phonon-assisted tunneling model also can be used to estimate the tunneling rate between ground states in  $\text{KTaO}_3$ . The tunnel integral  $J(R)$  was calculated using the double Morse potential and the relevant spectroscopic and lattice parameters. The amplitude of the inter-oxygen oscillation ( $\delta_{O-O}$ ) was estimated from the fitting pa-

rameters in Fig. 4.6. Using the ground state energy of the O-H oscillator, the tunneling rate between *minima* of the double well potential is estimated to be  $5 \times 10^5 \text{ s}^{-1}$  at room temperature. Results of this calculation are shown in Fig. 4.7. This implies an increase in tunneling rate of 4 orders of magnitude when the O-H LVM occupies the first vibrational level.

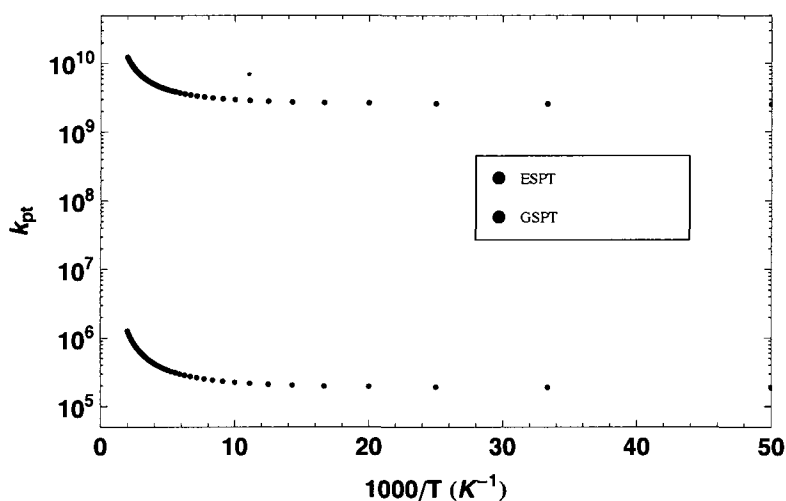


FIG. 4.7: Estimated ground state (GSPT) and excited state (ESPT) tunneling rates in  $\text{KTaO}_3$  according to Trakhtenberg's model.

## 4.5 Summary and Conclusions

In summary, the lifetimes of the O-H and O-D stretch modes in the perovskite oxide  $\text{KTaO}_3$  have been measured for the first time. Both stretch modes are exceptionally long lived and exhibit a large “reverse” isotope effect, due to a phonon-assisted tunneling process, which involves the O-Ta-O bending motion. An important finding of this chapter is that the tunneling events discussed here are *photon-stimulated*. Furthermore, when

compared to tunneling events between two ground states in a similar perovskite system, a rate increase of 7 orders of magnitude is observed, which is consistent with an estimated 4 order increase in  $\text{KTaO}_3$ . This implies that optical control or manipulation of proton transfer rates in oxide materials is practically feasible.

## CHAPTER 5

# Photon-Stimulated Proton Hopping in TiO<sub>2</sub>

Proton conduction in solid oxides is a fundamental process that has attracted considerable attention based on important developments and applications in hydrogen energy research. This process is usually observed at high temperatures (700-1000°C). The thermal energy is required to break the O-H bond so that the proton can move between oxygen atoms by the well-characterized Grotthuss mechanism [59] [9]. This requirement limits the practical application of devices. For example, in solid oxide fuel cells (SOFCs) high temperatures cause slow startup times, reduce operational lifetimes due to thermal stress, and require the use of expensive catalytic electrodes [60]. Therefore it is of great interest to develop mechanisms that can promote a high conductivity without the drawbacks associated with high temperature operation [13]. Indeed, in the early 1980s, Chen and co-workers found that electron radiation could induce the diffusion of protons and deuterons in TiO<sub>2</sub>—even at room temperature [61]. In the previous chapter, photon-stimulated H

tunneling in  $\text{KTaO}_3$  was observed to substantially increase the tunneling rate over ground state tunneling. From a theoretical standpoint, infrared photon stimulated H transport has been suggested in  $\text{ZnO}$  [12]; however direct experimental observation and characterization of this phenomenon in oxides are lacking.

## 5.1 Rutile $\text{TiO}_2$ : a Model System

The literature on hydrogen in rutile  $\text{TiO}_2$  is extensive going back to the late 1960s [62] [37]. In particular, H diffusion in has been studied by several groups and the diffusion coefficient has been well established [44] [63]. It has been found that diffusion along the  $c$  direction is highly efficient with low energy barriers, thus,  $\text{TiO}_2$  is particularly well suited to investigate the effect of IR photon absorption on proton transport.

Polarized IR absorption studies have shown that, in equilibrium, the O-H dipole is oriented perpendicular to the  $c$  axis [37] with a bond length of  $1.09 \text{ \AA}$  [64]. Long range migration consists of proton jumps between near-neighbor oxygen atoms in a helical path along the  $c$  axis direction and is indicated in Fig 5.1 [44].

As with  $\text{KTaO}_3$  and other oxides, the potential energy surface is successfully modeled with a Morse-type double-well potential. Figure 5.1b represents such an energy surface of a cross section of the  $c$  channel where the three oxygen sites shown represent the proton host (I), the adjacent near-neighbor site (II), and the site directly across the  $c$  channel (III). It is evident that the barrier is much higher along the O-H stretching direction than in the direction of an adjacent oxygen neighbor; thus, the preferred diffusion path involves a conformational transfer step consistent with a helical progression in the  $c$  direction. The horizontal lines in the left side well represent the ground and first vibrational states of the O-H stretch mode which play a key role in dictating how the proton

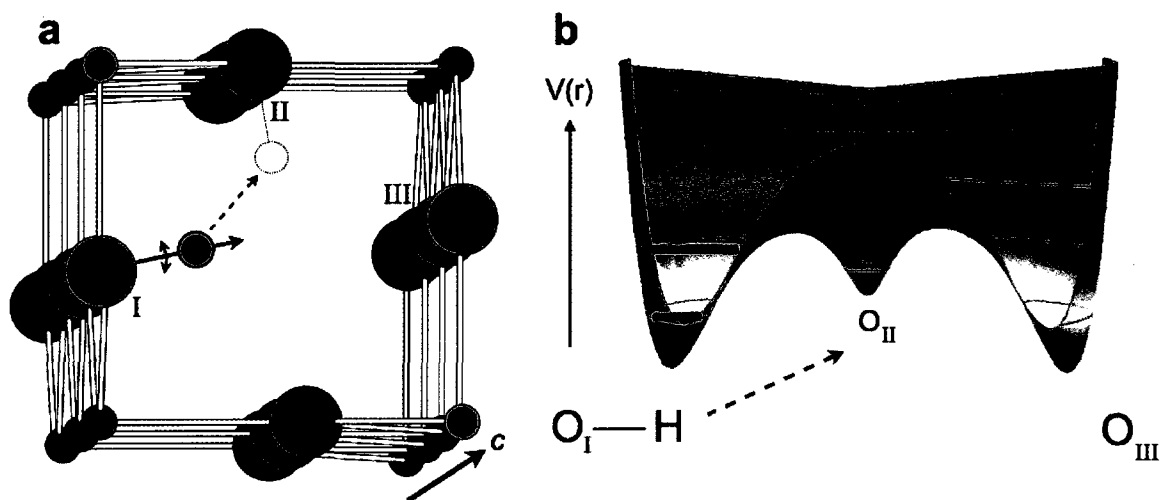


FIG. 5.1: Ionic configuration for the proton in the  $\text{TiO}_2$  lattice. (a) The rutile structure is shown here to emphasize the characteristic open  $c$  channel. Small arrows represent the vibration of the stretch and wag modes, while the dashed arrow indicated the reaction pathway for proton migration. (b) A schematic representation of the potential surface for the proton in the  $c$  channel. The horizontal lines depict vibrational levels for the O-H stretch mode.

traverses this energy surface. Therefore, a clear identification of the O-H decay process is needed for a complete understanding of proton transport in oxides.

## 5.2 Vibrational Lifetime Measurements

For this investigation, rutile (001)  $\text{TiO}_2$  single crystals were grown by the flame fusion method. They contained a high “as-grown” concentration of hydrogen and needed no further treatment. Deuterated samples were prepared by first annealing at  $1050^\circ\text{C}$  in vacuum for 24 h and then in  $\text{D}_2\text{O}$  vapor for up to 72 h.

The vibrational lifetimes are measured by transient bleaching spectroscopy in combination with high resolution ( $0.2\text{ cm}^{-1}$ ) FTIR absorption spectroscopy. The transient bleaching signal  $S_b$  for the O-D stretch mode is shown in Fig. 5.2a revealing a lifetime of

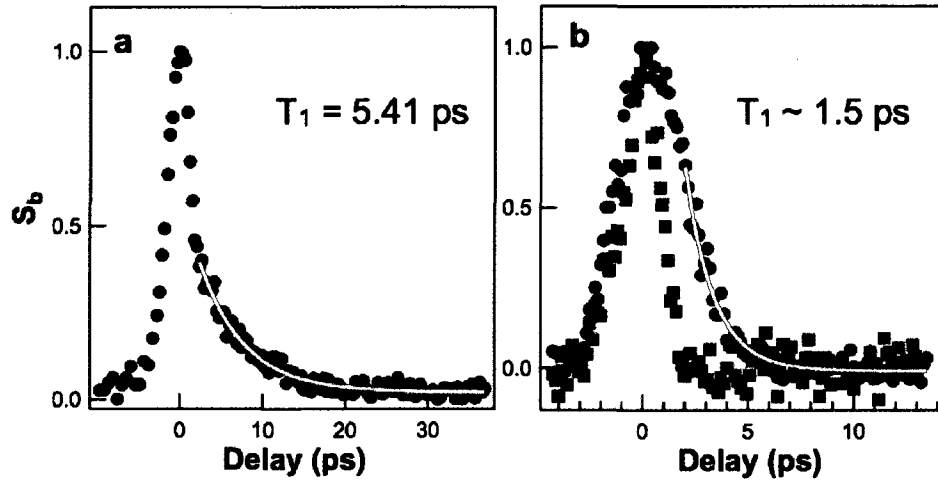


FIG. 5.2: Vibrational lifetimes of the O-D and O-D stretch modes. (a) The O-D transient bleaching signal is fit to a single exponential decay giving a lifetime of 5.41 ps and is in excellent agreement with the IR linewidth in Fig. 5.3. (b) The black circles indicate the O-H stretch mode measurement of approximately 1.5 ps. The gray squares indicate an off-resonant measurement representative of the laser pulse width. Note that the  $T_1$  values measured here are much shorter than in  $\text{KTaO}_3$ .

only  $T_1 = 5.41$  ps at 60 K. This is in excellent agreement with the measured IR linewidth  $\Gamma = 0.97\text{cm}^{-1}$  using the relation

$$T_1 = \frac{1}{2\pi c\Gamma} = 5.47 \text{ ps} \quad (5.1)$$

at 10 K, shown in Fig. 5.3a. The O-H lifetime was found to be  $T_1 \approx 1.75$  ps, which is close to the laser pulsewidth and consistent with the IR linewidth of  $\Gamma = 3.03\text{cm}^{-1}$ . Here equation (5.1) yields  $T_1 = 1.75$  ps. The agreement between the measured lifetimes and the IR linewidths indicates that inhomogeneous broadening mechanisms do not play a significant role in  $\text{TiO}_2$ .

The agreement between measured lifetimes and those extracted from the linewidth is important because it allows the extraction of the O-H lifetime at higher temperatures,

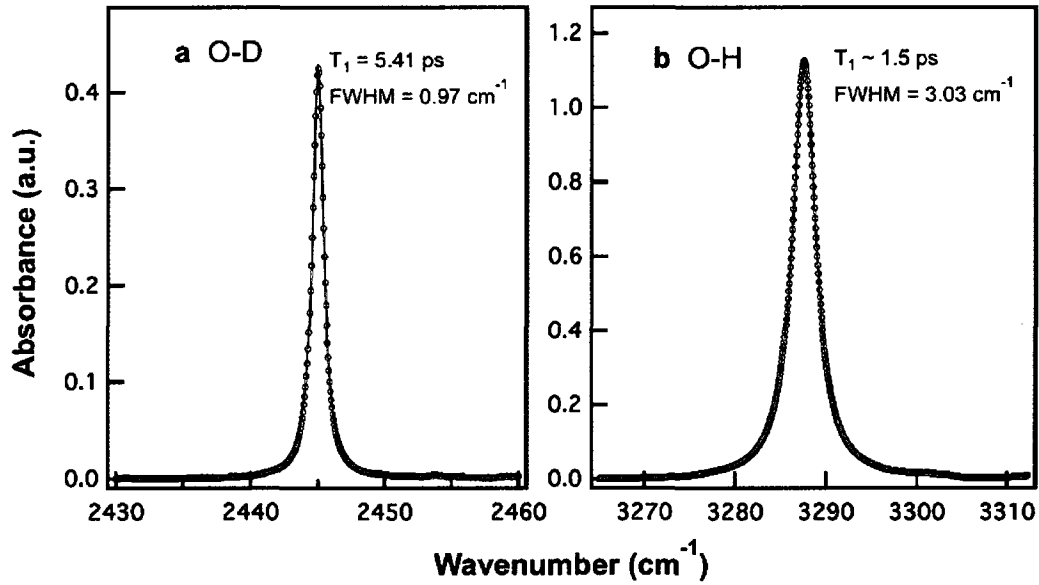


FIG. 5.3: Infrared absorption spectra of the O-D (a) and O-H (b) stretch modes in rutile  $\text{TiO}_2$ . The spectra are fitted with a Lorentzian line shape to yield FWHM values shown in the inset. These linewidths are in excellent agreement with the measured lifetimes using the relation in equation (5.1).

and the temperature dependence of the lifetimes provides valuable information about the proton dynamics. Figure 5.4 shows  $T_1$  as a function of temperature for the O-H and O-D stretch modes. The O-D lifetimes were measured directly by the transient bleaching technique, and the O-H lifetimes were obtained from the homogeneous linewidth ( $\Gamma$ ) where

$$\Gamma = \frac{1}{2\pi c T_1} + \frac{1}{\pi c T_2^*} \quad (5.2)$$

using the dephasing time  $T_2^*$  determined from the temperature dependence of the O-D linewidth. This assumption that both the O-H and O-D stretch modes have the same dephasing time is based on the fact that they both interact with the same low frequency phonon bath.

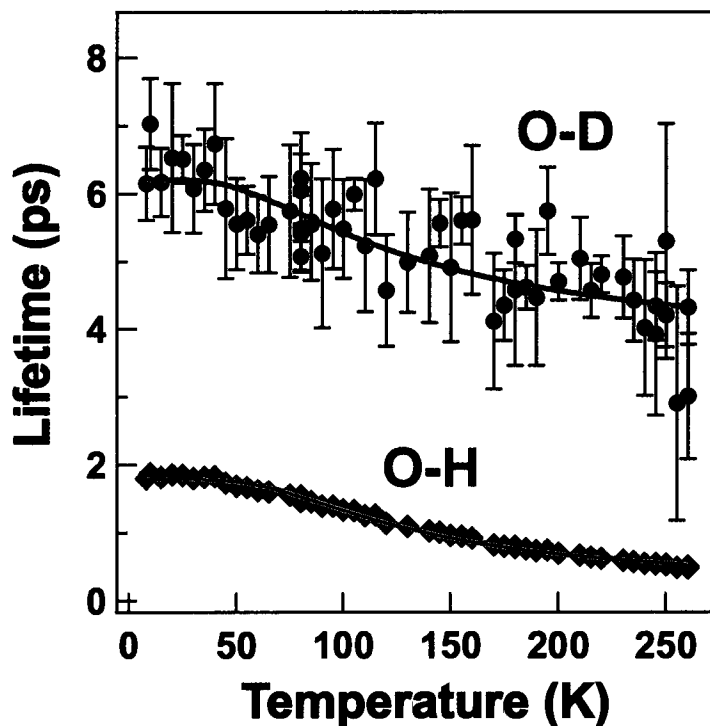


FIG. 5.4: Temperature dependence of the O-D lifetime (blue circles) along with the O-H lifetime (black diamonds) extracted from the vibrational linewidth. Both data sets are fitted to a model for a lattice-assisted proton transfer process.

According to the frequency-gap law, which relates H vibrational lifetime to the phonon decay order (number of phonons) of the local mode, the observed lifetime of  $\sim 2$  ps for O-H and  $\sim 5$  ps for O-D would correspond to a one or two phonon decay channel. The highest phonon frequencies in  $\text{TiO}_2$  are around  $850 \text{ cm}^{-1}$  [65], which would require at least four phonons for the proton decay. Additionally, the inclusion of a high frequency wag mode ( $1000\text{-}1400 \text{ cm}^{-1}$  for O-H) would still constitute a three-phonon decay process<sup>1</sup>. Moreover, the shape of the O-H and O-D lifetime temperature dependence

<sup>1</sup>Early calculations by Bates, Wang, and Perkins predicted wag modes at  $719$  and  $1400 \text{ cm}^{-1}$  in  $\text{TiO}_2$  [44]. In rutile  $\text{SnO}_2$ , first-principles calculations predict a value around  $1100 \text{ cm}^{-1}$ . Both are consistent with O-H bend modes in other oxides.

in Fig. 5.4 is not characteristic of multiphonon decay [66]. Therefore, this cannot be the dominant relaxation mechanism for the O-H and O-D stretch modes in  $\text{TiO}_2$ .

Other than multiphonon decay, vibrational relaxation can also occur via a proton rotation or transfer step - either by a classical “over the barrier” motion or by quantum tunneling from the excited state (as in  $\text{KTaO}_3$ ). Here, the later is unlikely because the observed isotope effect is too small. Tunneling would predict an isotope ratio of at least several hundreds based on a simple Wentzel-Kramers-Brillouin (WKB) estimate of the tunnel probabilities in a double-well potential. Thus, the most likely decay channel is a classical transport process.

### 5.3 Phonon-Assisted Hopping

As indicated in Fig. 5.1a, the reaction pathway involves a certain degree of coupling to the wagging motion of the O-H bond. Since the decay channel has been determined to be a classical transfer, the lifetime temperature dependence is fit to a model for a vibration-assisted proton hopping process described in section 2.3.3 where the time between jumps is given by

$$\tau = A u \Omega \exp[2u^2 \tanh(\hbar\Omega/4k_bT)], \quad (5.3)$$

where  $\Omega$  is the frequency of the assist phonon and  $A$  and  $u$  are constants related to the coupling strength [34]. Fits to the data, shown in Fig. 5.4, give assist phonon frequencies of  $\Omega = 372 \pm 8.6 \text{ cm}^{-1}$  for the O-H lifetime and  $\Omega = 286 \pm 62.3 \text{ cm}^{-1}$  for the O-D data. The other fit parameters for the O-H data are  $A = 2.4 \times 10^{-3} \pm 2.4 \times 10^{-4} \text{ ps}^2$  and  $u = 1.07 \times 0.015$ , and for the O-D data  $A = 0.12 \pm 0.045 \text{ ps}^2$  and  $u = 0.54 \pm 0.043$ . Both assist phonon frequencies are within the bulk phonon bands, but it is unlikely that both

isotopes transfer via different assist phonons. The ratio of the assist phonon frequencies is 1.31 and is in excellent agreement with the ratio of the O-H and O-D stretch mode frequencies (1.34), therefore indicating that the assist mode is also localized. The most likely candidate is the O-H wag mode, which is responsible for promoting the proton over the potential barrier. Additionally, it is possible that the low frequencies obtained here explain the lack of experimental observation of the wag modes in  $\text{TiO}_2$ . This assignment is consistent with the transverse direction of the diffusion path shown in Fig. 5.1, which requires the proton to move at an angle almost perpendicular to the  $c$  axis.

### 5.3.1 Energy Barrier

Further information on the transfer dynamics can be gained from an in-depth analysis of other hydrogen related vibrational modes. Figure 5.5 shows the linewidths of five vibrational modes plotted against photon (or stretch mode) energy. The three narrow linewidths are for the O-T, O-D, and O-H stretch modes. A relatively broad line at  $4355\text{ cm}^{-1}$  (see lower inset) uniquely associated with hydrogen [37] is likely a combination mode as reported by Soffer [67]. This assignment is consistent with stretch + wag combination modes found in other oxides [66] [53] as well as values based on first principles calculations. Additionally, in samples with a large hydrogen concentration we observe a new line at  $5920\text{ cm}^{-1}$  at 10 K, as shown in the upper inset in Fig. 5.5. This line is interpreted as the first overtone of the O-H stretch mode. Previous studies based on isotope shifts [62] and the calculated stretch-mode potential shape in rutile  $\text{SnO}_2$  [68] find a large anharmonicity of the O-H stretch. The O-H overtone proposed here requires an even greater anharmonicity and suggests that overtone data can be more sensitive to unusual anharmonic features than have been considered previously for the O-H potential. At lower energy, the

trium (O-T) stretch mode ( $2070.5 \text{ cm}^{-1}$ ) has been measured by Bates to have a width of  $1.2 \text{ cm}^{-1}$  at 10 K [62]. By comparison, the O-H and O-D absorbance spectra in the current work show linewidth values of a factor of 2 smaller than reported in Ref. [62]. Therefore, a more accurate value for the O-T linewidth is taken to be  $0.6 \text{ cm}^{-1}$ .

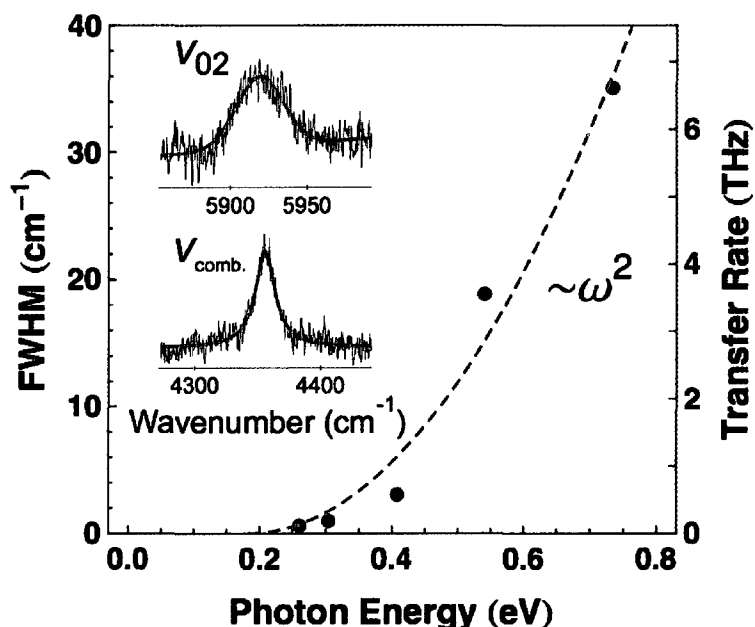


FIG. 5.5: Infrared linewidths (FWHM) for O-H, O-D, and O-T stretch modes in  $\text{TiO}_2$  measured at 10 K plotted against photon energy. The points shown are for the transitions  $\nu(\text{OT})_{01}$ ,  $\nu(\text{OD})_{01}$ ,  $\nu(\text{OH})_{01}$ ,  $\nu(\text{OH})_{\text{comb}}$ , and  $\nu(\text{OH})_{02}$  with increasing energy, where subscripts indicate the vibrational quantum number. Absorption lines for the O-H combination and overtone modes are shown in the inset.

The right hand axis of Fig. 5.5 represents the transfer rate determined from the linewidth using equation (5.1), which holds because all FTIR measurements were taken at 10 K so the dephasing term is negligible. The overall trend shows that the linewidths of the O-H related vibrational modes become broader with increasing energy. The broad linewidths ( $\Gamma$ ) of the higher levels are indicative of a very short upper-state lifetime and, hence a very high transfer rate ( $2\pi c\Gamma$ ). It is evident from the figure that the transfer rate

approaches zero at an excitation energy of  $\sim 0.2$  eV, which therefore corresponds to the barrier height for this transport process. This value is in agreement with the 0.2 to 0.4 eV barriers calculated by Wardle and co-workers for H reorientation and transfer steps in wurtzite ZnO—which has a slightly (20%) larger O-O separation than in TiO<sub>2</sub> [12]. Note that if one interprets the linewidth to be proportional to the density of proton transfer states, then as a rough approximation the data points in Fig. 5.5 can be fit with an  $\omega^2$  dependence consistent with the Debye model for the phonon density of states.

## 5.4 The Photo-Enhanced Hydrogen Transport Effect

The above measurements and analysis show that the absorption of a resonant IR photon can stimulate a proton to hop from one oxygen ion host to another. The lifetime measurements are a unique way to directly measure this photon-stimulated transport rate ( $1/T_1$ ). It is therefore worthwhile to compare the the IR-stimulated transfer rate with the standard thermally activated hopping rates obtained in TiO<sub>2</sub>. The experimental diffusion coefficient along the  $c$  channel in TiO<sub>2</sub> is given by the Arrhenius expression

$$D(T) = 1.8 \times 10^{-3} \exp[-0.59\text{eV}/k_b T] \quad (5.4)$$

from which a room temperature hopping rate can be approximated as  $D(300\text{K})/d^2 \approx 10^3 \text{ s}^{-1}$ , where  $d$  is the average jump distance (1.48 Å) [63]. By comparison, the room temperature IR-stimulated transfer rate (inverse lifetime) is  $\sim 10^{12} \text{ s}^{-1}$  – a giant enhancement representing an increase of 9 orders of magnitude! Such a dramatic enhancement is consistent with optical excitation of the proton to higher vibrational states above the energy barrier for transverse migration.

## 5.5 Summary and Conclusions

To summarize, measurements of the O-H and O-D vibrational lifetimes show that the room temperature hydrogen diffusion rate in rutile  $\text{TiO}_2$  can be enhanced by 9 orders of magnitude when stimulated by resonant infrared light. The analysis indicates that these LVMs are relatively unstable oscillations and quickly couple to a transverse wag mode with a much lower potential barrier of approximately 0.2 eV. This transverse oscillation then behaves as an assist phonon and promotes the proton to the adjacent oxygen host. The IR-stimulated proton transfer rate is on the order of a THz. It is reasonable to expect that IR-stimulated migration is possible in similar oxides (e.g.  $\text{SnO}_2$ ,  $\text{HfO}_2$ , and  $\text{ZnO}$ , among others) in which hydrogen is a highly mobile defect. Not only does this new fundamental insight into the microscopic dynamics of protons in  $\text{TiO}_2$  establish an important link between O-H vibrational decay and hydrogen transport but also it suggests a new method to enhance proton mobility in important applications ranging from fuel cells to hydrogen production.

# CHAPTER 6

## Summary and Outlook

### 6.1 Summary

This thesis presents a comprehensive experimental investigation into the relaxation dynamics of hydrogen related LVMs in solid oxides. The lifetimes and decay dynamics of hydrogen in two important representative oxides,  $\text{KTaO}_3$  and  $\text{TiO}_2$ , are investigated using picosecond pump-probe spectroscopy. This work is an extension to the oxides of a study on the lifetimes and relaxation mechanisms of hydrogen defects in silicon and germanium by Baozhou Sun.

In the perovskite oxide  $\text{KTaO}_3$  we have shown that the O-D stretch mode decays through a multiphonon interaction, but the O-H stretch mode has an additional contribution to the decay rate which is responsible for the shorter lifetime. This additional mechanism was identified as an excited-state phonon-assisted tunneling process involving the O-Ta-O bending mode. The tunneling rate has been determined from the decay rate measurements and is approximately  $10^{10}$  Hz at room temperature. This is remarkable

considering the tunneling rate between ground states in similar systems is typically only  $10^3$  Hz.

In rutile  $\text{TiO}_2$  the lifetimes are on the order of only a few picoseconds, which indicates that the decay process is very efficient. Here we have shown that when the O-H or O-D stretch mode is excited, it quickly couples to the wag mode which promotes it over the potential barrier to the adjacent oxide ion. Determination of this vibration-assisted hopping process implies that the lifetime measurements should be interpreted as inverse hop rates and allows one to compare the measured rate to that due to thermally activated diffusion. Similar to the  $\text{KTaO}_3$  case, we find a giant enhancement in hop rate of nine orders of magnitude.

The decay mechanisms in this work are found to be quite different than those found in the semiconductors (Si and Ge) where multiphonon relaxation dominates. We have identified proton tunneling and hopping as two new decay channels for hydrogen local modes in solid oxides. It is not unreasonable that similar mechanisms exist for some hydrogen defects in semiconductors as well. The primary difference and key insight for the oxides is that vibrational excitation is closely related to hydrogen migration or diffusion. It is reasonable that the low (or negligible) multiphonon decay rates found in oxides are partially responsible for the high proton conductivity observed in many such material structures.

In both  $\text{KTaO}_3$  and  $\text{TiO}_2$ , the observation that the absorption of a resonant IR photon can stimulate a tunneling or hopping event is quite remarkable. Absorption stimulated H migration has indeed been suggested in ZnO but until now has not been characterized experimentally in oxides. Moreover, the measured rate increases by up to a factor of  $10^9$  indicate how effective this effect might be in potential applications.

## 6.2 Outlook

This work establishes a solid foundation for a variety of future studies involving hydrogen defects in oxides. One particularly interesting direction would be to further explore the nature of photon-stimulated proton hopping. The rate enhancement observed at the microscopic level should translate to a dramatically increased diffusion coefficient on the bulk scale. Determination of the proton diffusion coefficient can be performed by monitoring the change in intensity of the O-H absorption peak due to an influx or out-diffusion of protons from the sample. As early as the mid-1980s, an interesting series of experiments at Oak Ridge National Lab reported radiation and electric field induced diffusion (REID) in  $\text{TiO}_2$ ,  $\text{MgO}$ ,  $\text{LiNbO}_3$ , and quartz where it was shown that electron bombardment can induce diffusion even at room temperature [61] [69] [70]. In these experiments an external electric field (2-3 kV/cm) was used to sweep the protons out of the sample as it was being irradiated. Using a similar external electric field, experiments with resonant infrared laser light could be realized and bulk diffusion could be observed and quantified with and without IR exposure. The high-power, tunable free electron laser at the nearby Thomas Jefferson National Lab can provide 100s of Watts of continuous wave IR laser light and is, thus, particularly well suited to perform such experiments.

Device applications for solid oxides such electrochemical cells rarely utilize oxides in single crystal form. Although single crystal rutile  $\text{TiO}_2$  would be a natural starting point for a macroscopic study of the photo-enhanced hydrogen transport effect, polycrystalline and ceramic oxides should also be considered. For example, a more “application oriented” polycrystalline oxide is doped  $\text{BaCeO}_3$  which can yield a proton conductivity of 0.02 S/cm at 600° C. An example FTIR spectra of this material is shown in Fig. 6.1. This figure shows a complicated and broad spectral feature in the expected range for O-H local

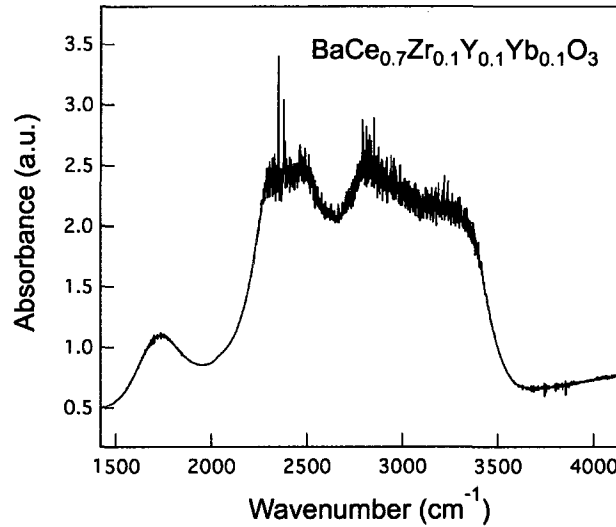


FIG. 6.1: Absorption spectra of the O-H stretching region of a polycrystalline electrolyte material.

modes, which is not surprising considering the complex sample composition.

Another fundamentally interesting system is the O-H complex in ZnO and other wide band-gap oxides where it has been established that hydrogen is a shallow donor [1]. In heavily doped ZnO samples, the absorption line associated with the O-H stretch mode ( $3326\text{ cm}^{-1}$ ) exhibits an asymmetry characteristic of a coupling between the local vibration and free electrons in the material. The donor nature of such defects indicates that the local vibration could couple electronically to the host crystal via this free carrier interaction [14]. This would present yet another new and interesting decay channel for hydrogen local modes. Preliminary pump-probe measurements of the  $3326\text{ cm}^{-1}$  line show a lifetime of approximately 20 ps from 10 to 80 K and are shown in Figs. 6.2 and 6.3. The asymmetry observed in the IR absorption spectra becomes less pronounced at low concentrations [71]; therefore, a concentration dependent study would provide valuable information regarding a possible electronic relaxation channel.

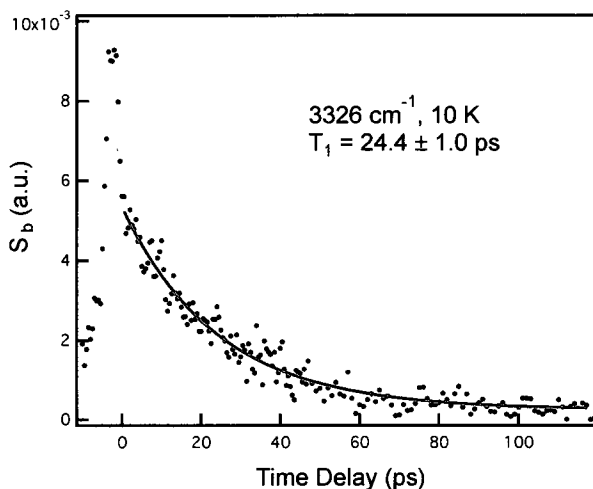


FIG. 6.2: Vibrational lifetime of the O-H stretch mode in ZnO at 10 K.

The hydrogen defects discussed above and those examined in this thesis are all interstitial – the proton sits between oxygen ions and does not occupy a regular lattice site. It would be interesting to investigate the nature of a vacancy associate O-H defect such as those found in MgO and ZnO. The charged  $V_{OH^-}$  and neutral  $V_{OH}$  defects in MgO have been identified spectroscopically [72] and exhibit relatively narrow linewidths. These complexes are associated with a Mg vacancy and identification of the vibrational decay mechanism could yield insight into a further structural dependence. Initial lifetime measurements for the  $V_{OH}$  stretch mode at  $3326\text{ cm}^{-1}$  show a relatively short lifetime and only a weak dependence on temperature (see Figs. 6.4 and 6.5). The lifetime of the  $V_{OD}$  stretch mode would complement this preliminary data and possibly allow one to determine the decay channel.

Although this thesis examines only two representative oxide materials, it is valuable to survey a broader collection of oxides so that one can draw expected similarities and pose further unanswered questions. Table 6.1 catalogues the vibrational frequency and

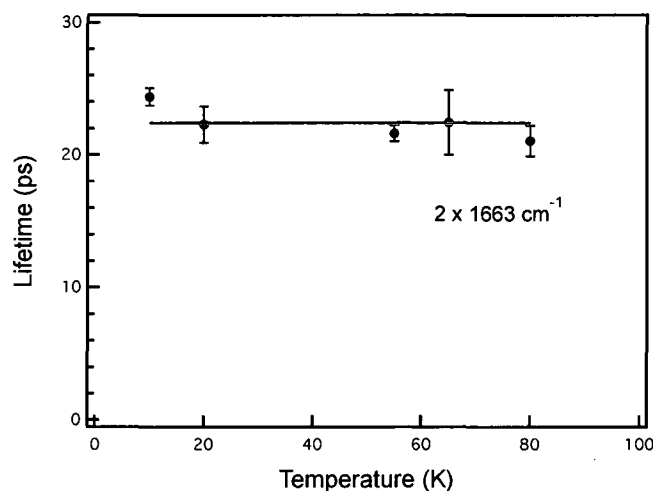


FIG. 6.3: Preliminary temperature dependence of the  $3326\text{ cm}^{-1}$  line in ZnO. Solid line is a fit to a two phonon decay process according to equation (2.13)

linewidth for a variety of important oxides. The table is divided into sections for each material or class of material. For example, the first five rows are all materials with the perovskite crystal structure. Based on the observation that most perovskites have similar O-H frequencies and linewidths, it is reasonable to assert that the vibrational lifetimes and decay mechanisms likely will be very similar. We can also make a similar assertion for  $\text{SnO}_2$  and  $\text{TiO}_2$ , which share the same rutile structure and have similar vibrational frequencies. It is interesting to note that if an O-H defect has a vibrational frequency near  $3500\text{ cm}^{-1}$  then its linewidth is usually very narrow (less than  $1\text{ cm}^{-1}$ ). Similarly, stretch modes centered around  $3200\text{-}3300\text{ cm}^{-1}$  usually exhibit linewidths of several wavenumbers. This observation points towards a frequency dependent decay rate.

Undoubtedly, the study of hydrogen defects in oxides is a vast and continually evolving field. The author hopes that this dissertation may contribute to this broad research arena and can complement a wide range of scientific investigations including those based on first-principle calculations, neutron scattering, or electrochemical techniques.

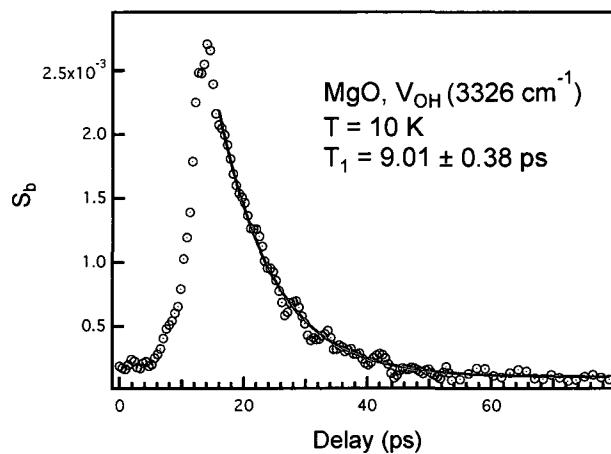


FIG. 6.4: Lifetime of the  $V_{OH}$  stretch mode in MgO measured at 10 K.

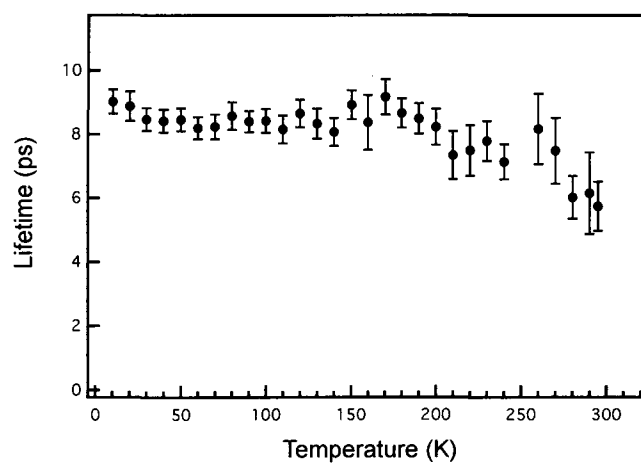


FIG. 6.5: Temperature dependence of the  $V_{OH}$  center in MgO.

Infrared Absorption Data for Hydrogen Related Stretch Modes in Oxides					
System	Defect	$\omega$ (cm <sup>-1</sup> )	FWHM (cm <sup>-1</sup> )	Temp (K)	Reference
KTaO <sub>3</sub>	O-H	3487 cm <sup>-1</sup>	0.117 cm <sup>-1</sup>	10 K	CW
	O-D	2576.8 cm <sup>-1</sup>	0.0966 cm <sup>-1</sup>	10 K	CW
SrTiO <sub>3</sub>	O-H	3514 cm <sup>-1</sup>	0.35 cm <sup>-1</sup>	4 K	[54]
	O-D	2596 cm <sup>-1</sup>	0.25 cm <sup>-1</sup>	4 K	[54]
BaTiO <sub>3</sub>	O-H	3485 cm <sup>-1</sup>	2.5 cm <sup>-1</sup>	300 K	[73]
	O-D	-	-	-	-
BaZrO <sub>3</sub>	O-H	3508 cm <sup>-1</sup>	-	-	[11]
	O-D	-	-	-	-
KNbO <sub>3</sub>	O-H	3504 cm <sup>-1</sup>	2.4 cm <sup>-1</sup>	300 K	[74]
ZnO	O-H	3326 cm <sup>-1</sup>	0.74 cm <sup>-1</sup>	10 K	[75], [76], CW
	O-D	2470 cm <sup>-1</sup>	-	10 K	[75], [76], CW
	Li-OH	3577.3 cm <sup>-1</sup>	0.4 cm <sup>-1</sup>	10 K	[77], [78]
	Li-OD	2644.5 cm <sup>-1</sup>	0.095 cm <sup>-1</sup>	10 K	[77]
	V <sub>Zn</sub> H <sub>2</sub> (1)	3312 cm <sup>-1</sup>	-	-	[76]
	V <sub>Zn</sub> H <sub>2</sub> (2)	3350 cm <sup>-1</sup>	-	-	[76]
	Cu-H	3191 cm <sup>-1</sup>	≈ 1 cm <sup>-1</sup>	10 K	[76]
	Unidentified	3335.5 cm <sup>-1</sup>	4.5 cm <sup>-1</sup>	80 K	CW
TiO <sub>2</sub>	O-H	3286.5 cm <sup>-1</sup>	7.0 cm <sup>-1</sup>	8 K	[62]
	O-D	2445 cm <sup>-1</sup>	2.0 cm <sup>-1</sup>	8 K	[62]
	O-T	2070.5 cm <sup>-1</sup>	1.2 cm <sup>-1</sup>	8 K	[62]
TiO <sub>2</sub>	O-H	3287 cm <sup>-1</sup>	3.033 cm <sup>-1</sup>	10 K	CW
	O-D	2445 cm <sup>-1</sup>	0.973 cm <sup>-1</sup>	10 K	CW
MgO	V <sub>OH</sub>	3326 cm <sup>-1</sup>	1.276 cm <sup>-1</sup>	10 K	CW
	V <sub>OH</sub> -	3297 cm <sup>-1</sup>	1.256 cm <sup>-1</sup>	10 K	CW
	V <sub>OD</sub>	2465 cm <sup>-1</sup>	-	-	[72]
	V <sub>OD</sub> -	2445 cm <sup>-1</sup>	-	-	[72]
SnO <sub>2</sub>	O-H	3254 cm <sup>-1</sup>	10 cm <sup>-1</sup>	300K	CW
	O-H	3261 cm <sup>-1</sup>	5 cm <sup>-1</sup>	80K	CW

TABLE 6.1: Known hydrogen complexes in various oxides including isotopic shifts, where available. Measurements are included from this thesis and are labeled as “current work” (CW). Those defects labeled with a V represent vacancy associates. For example, the V<sub>OH</sub> represents a OH group occupying the region adjacent to a Magnesium vacancy.

# **APPENDIX A**

## **Laser System Details**

### **A.1 Picosecond high power laser pulses**

The high power laser system used in this work consists of four essential components: an oscillator (or seed laser), a pump laser, a regenerative (REGEN) Ti:Sapphire amplifier, and a two-pass Ti:Sapphire amplifier. The oscillator, a Ti:Sapphire mode-locked Coherent MIRA (model 900-F), produces 200 fs pulses at 800 nm, and is pumped by a 4.07 W green beam from a diode laser (Coherent VERDI). A 527 nm, 16.5 W green beam from a Quantronix DARWIN Nd:YLF diode pumped laser is split and pumps the both the REGEN (15%) and the two-pass (85%) amplification stages. The seed pulse is stretched in time by a pair of gratings and is then switched into the REGEN amplification cavity at a repetition rate of 1 kHz by a Pockel's cell. Here an average power of 300 mW is achieved. The pulse is then switched out of the REGEN and passes into the two-pass amplification stage. The pulse is compressed by a second set of gratings and the final output power is 2.1 W at a pulse time of around 2 ps. The pulse repetition rate of the entire system is

synchronized to 1 kHz.

To experimentally characterize the pulse shape in time, an autocorrelation measurement can be performed. This involves splitting the TITAN output into two beams and varying the delay between them as they pass through a crystal capable of second harmonic generation (SHG). This SHG light will only be present when the two pulses overlap in time. By filtering out the fundamental 800 nm light and using a photodiode to record the blue 400 nm light as a function of delay between the two pulses, one can get a good estimate of the temporal pulse duration. The autocorrelation data is shown in Figure A.1. The data is fit to a “sech shape” pulse represented mathematically as  $I(t) = I_0 \text{sech}^2((t - t_0)/\tau)$ . The full width half maximum (FWHM) is found by multiplying the parameter  $\tau$  by 1.76. For this pulse shape, an autocorrelation factor of 0.65 multiplies the FWHM to yield a pulse duration of approximately 1.77 ps.

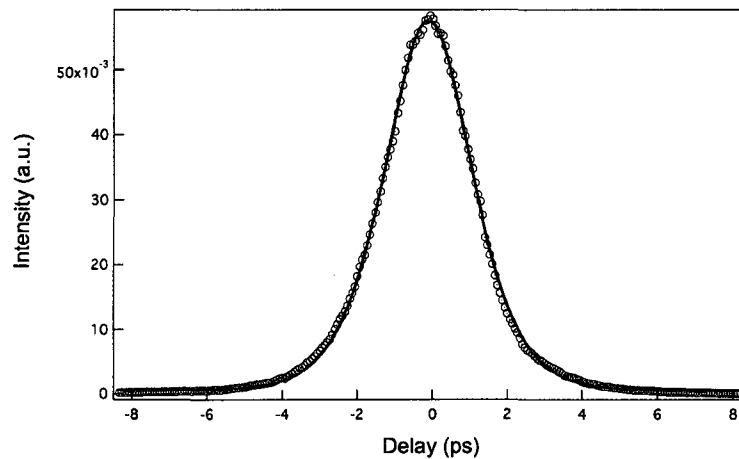


FIG. A.1: Autocorrelation measurement of the TITAN pulse time.

## A.2 Tunable infrared picosecond pulses

Absorption light by hydrogen LVMs in crystalline solids usually occurs around a frequency of  $3000 \text{ cm}^{-1}$ . In many material systems the bandwidth of such absorption resonances are very narrow. In order to probe the dynamics we require a light source that meets the following three requirements: narrow bandwidth, tunable, and picosecond pulse times.

In order to achieve tunable infrared picosecond laser pulses we use an optical parametric amplifier (OPA). Optical parametric amplification is a second order nonlinear optical process involving the mixing of three beams - a pump ( $\omega_p$ ), a signal ( $\omega_s$ ), and an idler ( $\omega_i$ ) which satisfy  $\omega_p = \omega_s + \omega_i$ . The three-wave mixing occurs in a non-centrosymmetric nonlinear crystal and is described by the second-order nonlinear polarizability of the medium given by

$$\vec{P}^{(2)} = \epsilon_o \bar{\chi}^{(2)} |E(z, t)|^2 \quad (\text{A.1})$$

where the electric field in the medium,  $E(z, t)$ , contains three spectral components

$$E(z, t) = E_p \cos(\omega_p t - k_p z) + E_s \cos(\omega_s t - k_s z) + E_i \cos(\omega_i t - k_i z) \quad (\text{A.2})$$

In order to achieve amplification there must be suitable optical feedback and gain. This nonlinear process can occur in a cavity with end mirrors of high reflectivity for  $\omega_s$  and  $\omega_i$  or only for  $\omega_s$  or  $\omega_i$ . These two configurations are known as doubly and singly resonant OPAs.

### A.2.1 Energy Conservation, Phase Matching and Tuning

For all nonlinear optical processes, energy and momentum ( $\hbar k$ ) must be conserved. For the three photon process described previously we have the following relations for the frequency ( $\omega$ ) and wavevector ( $k$ )

$$\omega_p = \omega_s + \omega_i$$

$$k_p = k_s + k_i$$

Under normal circumstances, the dispersion curves for light in the nonlinear medium do not allow for these conditions to be satisfied. However, it is possible to take advantage of the birefringence inherent to materials such as  $\beta$ -BaB<sub>2</sub>O<sub>4</sub> (BBO) and KTiOPO<sub>4</sub> (KTP) crystals. By rotating the crystals relative to the wave propagation direction it is now possible to meet the conservation requirements and tune the signal and the idler to the desired frequencies. The phase matching condition on the wavevectors of the three beams can be satisfied in two ways. The pump beam ( $k_p$ ) can be polarized perpendicular to both the signal and the idler (Type I) or it is also possible to have the signal or the idler polarized parallel to the pump (Type II).

### A.2.2 TOPAS

The OPA used in the present work is a Traveling-wave Optical Parametric Amplifier for Superfluorescence (TOPAS) made by Light Conversion. This section describes the basic layout of the TOPAS and gives the reader a basic understanding of the various stages involved in this doubly resonant parametric amplification device.

In the TOPAS the 800 nm pump beam (TITAN output) is divided up into three com-

ponents using two beam splitters. The weakest component (third part) is used for generation and initial amplification of superfluorescence (SFL) in the BBO nonlinear crystal (NC) through which it makes three passes. The weak SFL light is then directed onto a diffraction grating which spatially spreads the spectral components of this light and reflects them back in the direction of the NC acting as a seed for future amplification (the signal at  $\omega_s$ ). The spatial separation of the SFL spectral components allows selective amplification of a narrow bandwidth range by the “fourth-pass” beam - this is the reflected light off of the second beam splitter. Computer controlling of the crystal and grating angle allow a certain range of wavelengths to be selected for amplification. The fourth-pass joins the seed in space and time in the NC and becomes a pre-amplified beam. Any residual 800 nm pump light is filtered out and then the pre-amplified beam acts again as a seed for the final, more intense fifth-pass power amplification. The pump for the fifth-pass is from the first beam splitter located at the TOPAS input. Both the seed and pump are directed co-linearly through the NC where parametric amplification occurs. The idler is still a co-linear component of the output beam. The resulting beam is then filtered to remove the 800 nm pump light. The output beams (signal and idler) can now undergo difference frequency generation to extend the tuning range of the TOPAS. A schematic of the TOPAS is shown in Fig. A.2 from Ref. [79].

### **A.2.3 Difference Frequency Generation**

To further extend the tuning range of the TOPAS another second order nonlinear process called Difference Frequency Generation (DFG) is used. The principles of DFG are essentially the same as for parametric amplification described earlier. The primary difference is that there is no optical cavity for feedback and gain. The three wave mixing

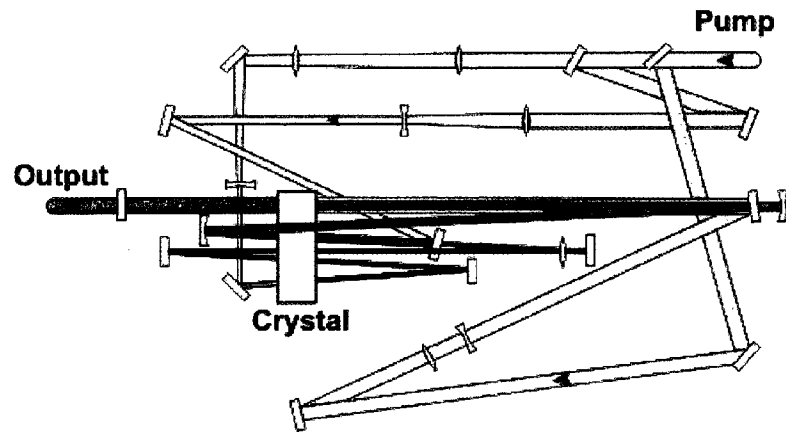


FIG. A.2: TOPAS optical layout.

involves the creation of a new frequency that is the difference between the two input frequencies. For example a signal of frequency  $7955.4 \text{ cm}^{-1}$  (  $1257.0 \text{ nm}$  ) and an idler at  $4621.9 \text{ cm}^{-1}$  (  $2163.6 \text{ nm}$  ) will result in a beam at  $3333.5 \text{ cm}^{-1}$  (  $3000 \text{ nm}$  ).

A housing containing two DFG crystals is mounted at the output of the TOPAS. A  $\text{AgGaS}_2$  crystal allows tuning from  $2.6 - 13 \mu\text{m}$  and a  $\text{GaSe}$  crystal allows tuning from  $4.5 - 22 \mu\text{m}$ . The crystal angle is controlled by the computer to reach the specified DFG output.

## BIBLIOGRAPHY

- [1] C. G. Van de Walle, *Phys. Rev. Lett.* **85**, 1012 (2000).
- [2] M. Grätzel, *Nature* **414**, 338 (2001).
- [3] C. Klingshirn, *ChemPhysChem* **8**, 782 (2007).
- [4] K. Xiong, J. Robertson, and S. J. Clark, *Journal of Applied Physics* **102**, 083710 (pages 13) (2007).
- [5] I. Satoh, J. Takaobushi, H. Tanaka, and T. Kawai, *Solid State Communications* **147**, 397 (2008), ISSN 0038-1098.
- [6] G. Enevoldsen, H. Pinto, A. Foster, M. Jensen, W. Hofer, B. Hammer, J. Lauritsen, and F. Besenbacher, *Phys. Rev. Lett.* **102**, 136103 (2009).
- [7] S. Li, Z. Zhang, D. Sheppard, B. Kay, J. White, Y. Du, I. Lyubinetsky, G. Henkelman, and Z. Dohnálek, *J. Am. Chem. Soc* **130**, 9080 (2008).
- [8] K. D. Kreuer, A. Fuchs, and J. Maier, *Solid State Ionics* **77**, 157 (1995).
- [9] C. de Grotthuss, *Ann. Chim* **58**, 54 (1806).
- [10] N. Sata, K. Hiramoto, M. Ishigame, S. Hosoya, N. Niimura, and S. Shin, *Physical Review B* **54**, 15795 (1996).
- [11] P. Sundell, M. Björketun, and G. Wahnström, *Physical Review B* **76**, 94301 (2007).

- [12] M. G. Wardle, J. P. Goss, and P. R. Briddon, *Physical Review Letters* **96**, 205504 (2006).
- [13] T. Norby, *Nature* **410**, 877 (2001).
- [14] B. Sun, Ph.D. thesis, College of William and Mary, Applied Science Department (2005).
- [15] D. West and S. K. Estreicher, *Phys. Rev. B* **75**, 075206 (2007).
- [16] B. Sun, G. A. Shi, S. V. S. N. Rao, M. Stavola, N. H. Tolk, S. K. Dixit, L. C. Feldman, and G. Lupke, *Phys. Rev. Lett.* **96**, 035501 (2006).
- [17] S. J. Jokela and M. D. McCluskey, *Physical Review B* **72**, 113201 (2005).
- [18] D. West and S. K. Estreicher, *Physical Review Letters* **96**, 115504 (2006).
- [19] P. M. Morse, *Phys. Rev.* **34**, 57 (1929).
- [20] M. Wöhlecke and L. Kovács, *Critical Reviews in Solid State & Materials Sciences* **26**, 1 (2001).
- [21] M. Budde, G. Lüpke, C. Parks Cheney, N. H. Tolk, and L. C. Feldman, *Phys. Rev. Lett.* **85**, 1452 (2000).
- [22] S. A. Egorov and J. L. Skinner, *The Journal of Chemical Physics* **103**, 1533 (1995).
- [23] A. Nitzan and J. Jortner, *Molecular Physics* **25**, 713 (1973).
- [24] A. Nitzan, S. Mukamel, and J. Jortner, *The Journal of Chemical Physics* **63**, 200 (1975).

- [25] A. Nitzan, S. Mukamel, and J. Jortner, *The Journal of Chemical Physics* **60**, 3929 (1974).
- [26] V. I. Gol'danskii, L. I. Trakhtenberg, and V. N. Fleurov, *Tunneling Phenomena in Chemical Physics* (Gordon and Breach Science Publishers, 1989).
- [27] L. I. Trakhtenberg, V. L. Klochikhin, and S. Y. Pshezhetsky, *Chemical Physics* **69**, 121 (1982).
- [28] L. Trakhtenberg and V. Klochikhin, *Chemical Physics* **232**, 175 (1998).
- [29] P. Leiderman, R. Gepshtein, I. Tsimberov, and D. Huppert, *Journal of Physical Chemistry B* **112**, 1232 (2008).
- [30] H. Böttger and V. V. Bryksin, *Hopping Conduction in Solids* (Akademie-Verlag, Berlin, 1985).
- [31] T. Tomoyose, *Phys. Rev. B* **43**, 13907 (1991).
- [32] T. Tomoyose, N. Shimoji, and K. Wakamura, *Journal of the Physical Society of Japan* **74**, 3011 (2005).
- [33] S. F. Fischer, G. L. Hofacher, and M. A. Ratner, *J. chem. Phys* **52**, 1934 (1970).
- [34] A. L. Samgin, *Solid State Ionics* **136-137**, 291 (2000), ISSN 0167-2738.
- [35] V. V. Krasnoholovets, P. M. Tomchuk, and S. P. Lukyanets, *Advances in Chemical Physics* (John Wiley & Sons, 2003), vol. 125, chap. 5.
- [36] P. R. Griffiths and J. A. de Haseth, *Fourier Transform Infrared Spectrometry* (Wiley, 2007), 2nd ed.

- [37] O. W. Johnson, W. D. Ohlsen, and P. I. Kingsbury, *Phys. Rev.* **175**, 1102 (1968).
- [38] K. Xiong and J. Robertson, *Applied Physics Letters* **85**, 2577 (2004).
- [39] Çetin Kiliç and A. Zunger, *Applied Physics Letters* **81**, 73 (2002).
- [40] R. González, I. Vergara, D. Cáceres, and Y. Chen, *Phys. Rev. B* **65**, 224108 (2002).
- [41] H. Iwahara, T. Yajima, T. Hibino, and H. Ushida, *Journal of the Electrochemical Society* **140**, 1687 (1993).
- [42] W.-K. Lee, A. Nowick, and L. Boatner, *Solid State Ionics* **18-19**, 989 (1986), ISSN 0167-2738.
- [43] D. M. Hannon, *Phys. Rev.* **164**, 366 (1967).
- [44] J. Bates, J. Wang, and R. Perkins, *Phys. Rev. B* **19**, 4130 (1979).
- [45] A. Nowick and A. Vaysleyb, *Solid State Ionics* **97**, 17 (1997).
- [46] H. J. Scheel, *Journal of Crystal Growth* **211**, 1 (2000), ISSN 0022-0248.
- [47] M. Benoit, D. Marx, and M. Parrinello, *Nature* **392**, 258 (1998).
- [48] Y. Cha, C. Murray, and J. Klinman, *Science* **243**, 1325 (1989).
- [49] H. Iwahara, *Solid State Ionics* **86-88**, 9 (1996), ISSN 0167-2738, proceedings of the 10th International Conference on Solid State Ionics.
- [50] I. Kuskovsky, B. Lim, and A. Nowick, *Physical Review B* **60**, 3713 (1999).
- [51] P. Johanssen, *J. Phys.: Condens. Matter* **10**, 2241 (1998).

- [52] M. Budde, G. Lüpke, E. Chen, X. Zhang, N. H. Tolk, L. C. Feldman, E. Tarhan, A. K. Ramdas, and M. Stavola, *Phys. Rev. Lett.* **87**, 145501 (2001).
- [53] A. Grone and S. Kapphan, *Journal of Physics: Condensed Matter* **7**, 3051 (1995).
- [54] G. Weber, S. Kapphan, and M. Wöhlecke, *Phys. Rev. B* **34**, 8406 (1986).
- [55] A. Gröne and S. Kapphan, *Journal of Physics and Chemistry of Solids* **56**, 687 (1995).
- [56] C. Perry, R. Currat, H. Buhay, R. Migoni, W. Stirling, and J. Axe, *Phys. Rev. B* **39**, 8666 (1989).
- [57] D. J. Singh, *Phys. Rev. B* **53**, 176 (1996).
- [58] E. Foley, A. Kam, J. Lyding, and P. Avouris, *Physical Review Letters* **80**, 1336 (1998).
- [59] R. Hempelmann, *Physica B: Condensed Matter* **226**, 72 (1996), ISSN 0921-4526.
- [60] H. Matsumoto, I. Nomura, S. Okada, and T. Ishihara, *Solid State Ionics* **179**, 1486 (2008), ISSN 0167-2738.
- [61] Y. Chen, R. Gonzalez, and K. Tsang, *Physical Review Letters* **53**, 1077 (1984).
- [62] J. Bates and R. Perkins, *Phys. Rev. B* **16**, 3713 (1977).
- [63] O. W. Johnson, S. Paek, and J. W. DeFord, *Journal of Applied Physics* **46**, 1026 (1975).
- [64] P.-O. Andersson, E. L. Kollberg, and A. Jelenski, *Phys. Rev. B* **8**, 4956 (1973).

- [65] R. Sikora, *Journal of Physics and Chemistry of Solids* **66**, 1069 (2005), ISSN 0022-3697.
- [66] E. J. Spahr, L. Wen, M. Stavola, L. A. Boatner, L. C. Feldman, N. H. Tolk, and G. Lüpke, *Phys. Rev. Lett.* **102**, 075506 (pages 4) (2009).
- [67] B. Soffer, *The Journal of Chemical Physics* **35**, 940 (1961).
- [68] J. B. Varley, A. Janotti, A. K. Singh, and C. G. Van de Walle, *Phys. Rev. B* **79**, 245206 (2009).
- [69] R. Gonzalez, Y. Chen, and K. L. Tsang, *Phys. Rev. B* **26**, 4637 (1982).
- [70] R. Gonzalez and Y. Chen, *Journal of Physics: Condensed Matter* **14**, R1143 (2002).
- [71] G. A. Shi, M. Saboktakin, M. Stavola, and S. J. Pearton, *Applied Physics Letters* **85**, 5601 (2004).
- [72] B. Henderson, J. L. Kolopus, and W. P. Unruh, *The Journal of Chemical Physics* **55**, 3519 (1971).
- [73] M. Wöhlecke and L. Kovács, *Critical Reviews in Solid State and Materials Sciences* **26**, 1 (2001).
- [74] A. FBrster, H. Hesse, and S. Kapphan, *Solid State Communications* **57**, 373 (1986).
- [75] M. D. McCluskey, S. J. Jokela, and W. M. Hlaing Oo, *Physica B: Condensed Matter* **376-377**, 690 (2006).
- [76] E. V. Lavrov, F. Bornert, and J. Weber, *Physica B: Condensed Matter* **401-402**, 366 (2007).

- [77] G. A. Shi, M. Stavola, and W. B. Fowler, *Phys. Rev. B* **73**, 081201 (2006).
- [78] L. E. Halliburton, L. Wang, L. Bai, N. Y. Garces, N. C. Giles, M. J. Callahan, and B. Wang, *Journal of Applied Physics* **96**, 7168 (2004).
- [79] (2010), URL <http://www.lightcon.com/index.php?TOPAS>.

## VITA

### Erik J. Spahr

Erik Spahr was born on November 16, 1981 in Waynesboro, Virginia. He attended Mary Washington College where, in May 2004, he received a Bachelors of Science in Physics. He initially started graduate school at the Colorado School of Mines, but then transferred to the College of William and Mary's graduate program in January 2006. He received his Masters in Physics from William and Mary in May 2007. On September 20, 2009 he married his wife, Aiyana, in Richmond, Virginia. Spahr completed his Ph.D. in Physics in August 2010 and that same year co-founded Phenom Technologies, Inc. with Dr. Gunter Lüpke to pursue proof of concept studies of the photo-enhanced hydrogen transport effect. He is a member of the American Physical Society and the Optical Society of America.